TNF Superfamily Member 14 Drives Post-Influenza Depletion of Alveolar Macrophages Enabling Secondary Pneumococcal Pneumonia

Christina Malainou^{1,2,3}, Christin Peteranderl¹, Maximiliano Ruben Ferrero^{2,3,4,5}, Ana Ivonne Vazquez-Armendariz^{1,6}, Ioannis Alexopoulos^{1,2,3}, Katharina Franz^{1,2,3}, Klara Knippenberg^{1,2,3}, Julian Better^{1,2,3,7}, Mohammad Estiri^{1,2,3}, Cheng-Yu Wu^{3,7}, Hendrik Schultheis^{3,5}, Judith Bushe⁸, Maria-Luisa del Rio⁹, Jose Ignacio Rodriguez-Barbosa⁹, Klaus Pfeffer¹⁰, Stefan Günther^{3,5}, Mario Looso^{3,5}, Achim Dieter Gruber⁸, István Vadász^{2,3,7}, Ulrich Matt^{1,2,3}, Susanne Herold^{1,2,3}

- 1 Department of Medicine V, Internal Medicine, Infectious Diseases and Infection Control, Universities of Giessen and Marburg Lung Center (UGMLC), member of the German Center for Lung Research (DZL), member of the German Center for Infection Research (DZIF), Justus Liebig University Giessen, Giessen, Germany.
- 2 Institute of Lung Health (ILH), Justus Liebig University Giessen, Giessen, Germany.
- 3 Excellence Cluster Cardio-Pulmonary Institute (CPI), Hessen, Germany.
- 4 Biomedicine Research Institute of Buenos Aires CONICET-Partner Institute of the Max Planck Society (IBioBA-MPSP) Buenos Aires, Argentina.
- 5 Max-Planck-Institute for Heart and Lung Research, Bad Nauheim, Germany.
- 6 University of Bonn, Transdisciplinary Research Area Life and Health, Organoid Biology, Life & Medical Sciences Institute, Bonn, Germany.
- 7 Department of Internal Medicine II, Universities of Giessen and Marburg Lung Center, University Hospital Giessen, Justus Liebig University, Member of the German Center for Lung Research (DZL), Giessen, Germany.
- 8 Department of Veterinary Pathology, Free University Berlin, Berlin, Germany.

9 Transplantation Immunobiology Section, Institute of Molecular Biology, Genomics

and Proteomics (INBIOMIC), University of León, León, Spain.

10 Institute of Medical Microbiology and Hospital Hygiene, Heinrich Heine University

Düsseldorf, Düsseldorf, Germany.

Address correspondence to: Susanne Herold, Department of Medicine V, Internal

Medicine, Infectious Diseases and Infection Control, University Hospital Giessen and

Marburg, Justus-Liebig-University, Klinikstrasse 33, D-35392 Giessen, Germany.

Phone: +49-(0)641-985-57061; E-mail: Susanne.Herold@innere.med.uni-giessen.de.

The authors have declared that no conflict of interest exists.

Key words: influenza A virus, pneumonia, alveolar macrophages, TNF superfamily,

Streptococcus pneumoniae

Abstract

1

2

3

4

5

6

7

8

9

10

11

12

13

14

15

16

17

18

19

20

21

Secondary bacterial infection, often caused by Streptococcus pneumoniae (Spn), is one of the most frequent and severe complications of influenza A virus (IAV)-induced pneumonia. Phenotyping of the pulmonary immune cell landscape after IAV infection revealed a substantial depletion of the tissue-resident alveolar macrophage (TR-AM) population at day 7, which was associated with increased susceptibility to Spn outgrowth. To elucidate the molecular mechanisms underlying TR-AM depletion, and to define putative targets for treatment, we combined single-cell transcriptomics and cell-specific PCR profiling in an unbiased manner, using in vivo models of IAV infection and IAV/Spn co-infection. The TNF superfamily 14 (TNFSF14) ligand-receptor axis was revealed as the driving force behind post-influenza TR-AM death during the early infection phase, enabling the transition to pneumococcal pneumonia, while intrapulmonary transfer of genetically modified TR-AMs and antibody-mediated neutralization of specific pathway components alleviated disease severity. With a mainly neutrophilic expression and a high abundance in the bronchoalveolar fluid (BALF) of patients with severe virus-induced ARDS, TNFSF14 emerged as a key determinant of virus-driven lung injury. Targeting the TNFSF14-mediated intercellular communication network in the virus-infected lung can, therefore, improve host defense, minimizing the risk of subsequent bacterial pneumonia, and ameliorating disease outcome.

Introduction

22

23

24

25

26

27

28

29

30

31

32

33

34

35

36

37

38

39

40

41

42

43

44

45

46

47

Bacterial pneumonia, often caused by Spn, is one of the most common complications of primary IAV infection, increasing the risk of death, intensive care unit (ICU) admission, and requirement for mechanical ventilation (1). While strengthening host defense offers a potential alternative to antibiotics amid globally rising resistance, progress is limited by poor understanding of the immune mechanisms behind severe influenza and the transition to post-viral bacterial pneumonia. Among these, virusinduced depletion of the TR-AM pool is considered a key factor in promoting secondary bacterial pneumonia, alongside epithelial damage, influx of pro-inflammatory cells, and impaired mechanical clearance (2, 3). TR-AM numbers remain relatively unchanged during homeostasis, with the main function of the cells being surfactant clearance and containment of minor infections (4). This tolerogenic programming, however, can be overridden by abundant viral presence, leading to a pro-inflammatory phenotypic switch, including extensive cytokine release and phagocytosis of viral particles and apoptotic cells (4, 5). TR-AM loss, often observed after severe infection and notoriously known as the 'TR-AM disappearance reaction' (6, 7), dramatically increases IAV-associated mortality (8, 9), the specific pathomechanisms behind it remain, however, elusive. The TNFSF involves a variety of structurally homologous ligands with multiple functions during development, homeostasis, and tissue response to injury (10). TNFSF14 or LIGHT [homologous to lymphotoxins, exhibits inducible expression and competes with Herpes Simplex Virus (HSV) glycoprotein D for herpes virus entry mediator (HVEM), a receptor expressed by T-lymphocytes] is widely expressed on cells of the hematopoietic compartment (11, 12). In the lung, TNFSF14 has been associated with airway remodeling in asthma, idiopathic pulmonary fibrosis, systemic sclerosis models (13, 14), and more recently, with disease severity in covid-19 (15,

48 16). Still, little is known regarding the pathomechanistic role of TNFSF14 in virus-49 induced pneumonia. TNFSF14 binds to three different receptors; type I transmembrane lymphotoxin beta 50 receptor (LTbR), HVEM, also known as TNF receptor superfamily 14 (TNFRSF14), 51 52 and decoy receptor 3 (DcR3), which is only found in primates (10). TNFSF14 receptors have a broad distribution on immune, stromal, and parenchymal cells (17), and 53 orchestrate distinct intracellular pathways. The outcome of TNFSF14 crosslinking to 54 55 its receptors, therefore, heavily relies on disease context and microenvironmental cues (10). Here, we sought to investigate the molecular mechanisms of post-influenza TR-56 57 AM loss and its consequences for host defense in a model of IAV and IAV/Spn infection, aiming at identifying any putative targets for immune-based pneumonia 58 59 treatment options.

Results

61

62

64

65

66

67

68

69

70

71

72

73

74

75

76

77

78

79

80

81

82

83

84

85

86

Severe IAV infection increases susceptibility to secondary pneumococcal

63 infection

To elucidate the pathomechanisms behind TR-AM death after severe IAV infection and its effect on the establishment of secondary bacterial pneumonia, we established a robust co-infection model (Figure 1A). Disease severity after viral, bacterial, or coinfection was shown to vary in a pathogen- and infection dose-dependent manner. Orotratracheal (o.t.) infection of C57BL/6 wild-type (wt) mice with 500 foci-forming units (ffu) IAV A/PR/8/34 decreased mouse survival by 50% 14 days after infection, whereas intranasal infection with 2000 colony-forming units (cfu) Spn Serotype 3 (PN36 NCTC7978) did not affect survival (Figure 1B) or weight loss (Figure 1C). However, IAV infection seven days prior to pneumococcal infection caused massive leukocyte infiltration (Figure 1, D-G) and a 100% lethal outcome (Figure 1B). Upon use of lower IAV and Spn doses (250ffu/20cfu on day 7 post-IAV infection, pi), average survival was calculated at 37.5% (Figure 1B). Despite the low infection doses, bacterial load in the BALF of previously IAV-infected mice was remarkably high 48h after pneumococcal infection, whereas PBS-pretreated mice completely cleared the infection (Figure 1H), suggesting an IAV-associated impaired immune response against invading Spn. We, therefore, characterized the leukocyte landscape of the IAV-infected lung, as distinct immune cell populations and their interactions can differentially affect post-influenza bacterial clearance (3, 18, 19). Flow cytometry profiling of BALF leukocytes (gating strategy depicted in Supplemental Figure 1A) revealed cell-specific kinetics over the infection course (Figure 11). Of note, BALF TR-AM numbers, which started significantly declining on day 3 pi, were almost completely depleted between 7-11 days pi (Figure 1J). Similar results were shown for lung-tissue leukocytes (gating strategy in Supplemental Figure 1B), which could not be acquired through BAL due to their sessile

nature (Supplemental Figure 2A) (20) or extra-alveolar location (Supplemental Figure 2, B-M). Upon co-infection, BALF bacterial outgrowth was observed 24h after pneumococcal infection (Figure 1K), coinciding with the period of maximum TR-AM depletion, despite the abundant presence of bone marrow-derived macrophages (BMDM). TR-AMs presented higher Spn phagocytosis capacity (Figure 1L) and no inferiority in killing capacity to the infection-driven pro-inflammatory BMDM (Figure 1M), highlighting the importance of TR-AM preservation for maintaining intact host defense. To address this, we sought to identify the molecular underpinnings of post-influenza TR-AM death.

Post-influenza TR-AM death involves the activation of caspase-8

Direct viral infection can lead to epithelial cell apoptosis in IAV-induced pneumonia (21, 22), posing the question whether this also drives post-IAV TR-AM depletion. Flow cytometry analysis revealed only a small number of IAV-infected TR-AMs (quantified by virus hemagglutinin (HA) expression) with no significant increase over the infection course (Figure 2A). The majority of HA-negative cells had been depleted by day 7 pi (Figure 2A), implying the involvement of a different mechanism with a much higher impact. In accordance with that, when naïve TR-AMs were ex vivo treated with virus-and cell-free BALF from IAV-infected mice (iBALF) from day 7 pi (day of maximum depletion), we observed a significant decrease in TR-AM survival (Figure 2B) and an increase in caspase-3/7 (Figure 2C) and caspase-8 activity (Figure 2D). Transcriptome analysis of flow-sorted HA-negative TR-AMs on days 3 and 7 pi based on a cell-death gene array revealed an upregulation of multiple apoptosis-related genes, such as Bax, Cd40lg, and Cflar, and necrosis-related genes, including Bmf, Commd4, Defb1, and Parp1 (Figure 2E and Supplemental Material, Cell death arrays wt data). Fold changes of upregulated genes did not differ significantly from baseline, as cell death is mainly

regulated on a (post-)translational level (23). Concomitant flow cytometry analysis, however, revealed a remarkable increase in apoptotic TR-AMs over the infection course (Figure 2F, gating strategy in Supplemental Figure 3A). As a result, we raised the question whether apoptosis inhibition would improve TR-AM survival. Following pre-incubation with a non-toxic concentration (Supplemental Figure 3, B-C) of 50µM of a specific caspase-3 (Z-DEVD-FMK) or caspase-8 inhibitor (Z-IETD-FMK), naïve TR-AMs were treated with iBALF. Whereas caspase-3 inhibition only showed a negligible protective effect, TR-AM death was completely abrogated in the caspase-8 inhibition group (Figure 2G). When mice were treated with daily subcutaneous (s.c.) injections of the caspase-8 inhibitor (schematic of experimental layout in Figure 2H), an attenuated weight loss was observed up to day 7 pi (Figure 2I). Caspase-8 inhibition fully protected the TR-AM pool on day 3 pi (Figure 2J), without affecting viral titers (Figure 2K), and significantly mitigated TR-AM loss on day 7 pi (Figure 2L). Caspase-8 is a known orchestrator of cell death, typically activated upon the crosslinking of a soluble ligand to a death receptor (24), which, together with the primarily virusindependent TR-AM apoptosis, hinted at a soluble ligand as a driver of TR-AM death.

129

130

131

132

133

134

135

136

137

138

113

114

115

116

117

118

119

120

121

122

123

124

125

126

127

128

IAV pneumonia sensitizes TR-AMs to TNFSF14 ligation

Death-inducing members of the TNFSF have been associated with promoting alveolar epithelial cell death and driving post-IAV lung injury (18, 25, 26). As such, we hypothesized that a TNFSF member could be involved in post-IAV TR-AM death and analyzed gene expression patterns of receptors and ligands belonging to the TNFSF signaling network in flow-sorted, HA-negative, TR-AMs from mock-infected and infected mice on days 3 and 7 pi. TNFRSF14, a receptor for TNFSF14, showed a significant upregulation at both time points (Figure 3A and Supplemental material, TNF signaling arrays wt data). TNFRSF14 demonstrated a significant increase in mRNA

and cell surface protein expression levels over the infection course and after ex vivo TR-AM stimulation with iBALF (Figure 3, B-D). LTbR, the competitor receptor for TNFSF14, presented no changes in transcriptional regulation, yet a distinct increase in protein expression (Figure 3, B-C, and E). On day 3 pi, the majority of TR-AMs stained positive for TNFSF14 receptors (Supplemental Figure 4A). Regarding TNFSF ligand expression, we confirmed previous reports on IAV-induced upregulation of Tnfsf10 in lung macrophages (25, 26), whereas Tnfsf15 and Tnfsf14 were moderately increased (Figure 3F and Supplemental material, TNF signaling arrays wt data). Overall, severe IAV infection was linked to a total TNFSF14 increase in the mouse lung, as shown by IHC (Figure 3G), qPCR (Figure 3H), and ELISA (Figure 3I). In accordance with that, we observed a significant increase in soluble TNFSF14 in the BALF of patients with influenza or COVID-19 acute respiratory distress syndrome (ARDS), compared to control patients who underwent routine bronchoscopy for diagnostic purposes and revealed normal BALF cellularity (Figure 3J). Based on the distinct kinetics of the two TNFSF14 receptors, we aimed at dissecting any differential roles in post-influenza TR-AM fate. Anti-LTbR TR-AM pre-treatment significantly attenuated the increase in caspase-3/7 activity after iBALF treatment, as opposed to the anti-TNFRSF14 and isotype control groups (Figure 3K). Similar results were observed when we treated naïve wt, Tnfrsf14-/-, and Ltbr-/-TR-AMs with iBALF (Figure 3L), indicating a potential protective effect against soluble death-inducing ligands in the absence of LTbR. In accordance with that, IAV-infected Ltbr/- mice demonstrated a less dramatic drop in TR-AM numbers, compared to wt and *Tnfrsf14*^{-/-} mice (Figure 3M), as well as an overall attenuated weight loss on days 7 and 8 pi (Figure 3N). The distinct effects of the two receptors on TR-AM survival and the upregulation of the common TNFSF14 ligand in IAV-infected lungs led us to examine TNFSF14 closer.

139

140

141

142

143

144

145

146

147

148

149

150

151

152

153

154

155

156

157

158

159

160

161

162

TNFSF14 drives the depletion of the TR-AM pool in IAV-induced pneumonia

165

166

167

168

169

170

171

172

173

174

175

176

177

178

179

180

181

182

183

184

185

186

187

188

189

190

To test whether TNFSF14 only induced apoptosis in a subpopulation of TR-AMs. TNFSF14 receptor expression on TR-AM surface was combined with apoptosis staining (annexin V/7-aminoactinomycin, 7-AAD) at different time points after infection. TNFSF14 receptor-expressing cells comprised approximately 80% of apoptotic TR-AMs on day 3 pi (Supplemental Figure 4B). When we compared TR-AMs regarding apoptosis induction based on TNFSF14 receptor expression, TNFSF14 receptorpositive TR-AMs presented significantly higher apoptosis rates on days 3 and 8 pi, compared to LTbR-TNFRSF14 cells (Figure 4A). To test whether TNFSF14 could directly induce TR-AM death, we treated naïve murine (Figure 4B) and human BALF TR-AMs (Figure 4C) with different concentrations of recombinant TNFSF14 (rTNFSF14) for 24h. Treatment with 500ng/ml rTNFSF14 led to an average of 25-35% decrease in TR-AM survival compared to the control PBS/BSA group (Figure 4, B-C) and an increase in caspase-3/7 activity, which was even more pronounced when the same setup was performed with day 3 TR-AMs (Figure 4D). Unlike TR-AMs, epithelial cells, which present a basolateral LTbR and a non-preferential, cytoplasmic TNFRSF14 expression pattern (Supplemental Figure 4, D-G), and are also exposed to homotrimeric, active (27), TNFSF14 in the BALF (Supplemental Figure 4, H-I), did not succumb to TNFSF14-induced apoptosis (Supplemental Figure 4C), mirroring the diverse roles of TNFSF14 signaling, based on cell type and receptor availability. O.t. application of rTNFSF14 to IAV-infected mice (schematics in Figure 4E) led to a significant increase in the number of annexin V+ TR-AMs (Figure 4F) and further reduced the already diminished BALF and lavaged-lung-tissue TR-AM numbers on day 3 pi (Figure 4, G-H), compared to PBS-treated, IAV-infected controls. No differences could be detected in the numbers of other leukocyte populations, based on rTNFSF14 treatment (Supplemental Figure 5, A-E). Concomitantly, TR-AM loss was completely

abrogated in the BALF and lavaged lung tissue of *Tnfsf14-/-* mice (Figure 5, A-B). This result could not be reproduced in *Tnfsf10*^{-/-} mice (Supplemental Figure 5F), despite TNFSF10 being one of the pro-apoptotic ligands highly expressed in the BALF after IAV infection (25, 26), suggesting a ligand-specific induction of TR-AM apoptosis. Flow-sorted *Tnfsf14-/-* TR-AMs showed lower induction of apoptosis, necrosis, and autophagy-related genes (Figure 5, C-D, Supplemental Figure 5, G-J, Supplemental material, Cell death arrays *Tnfsf14* ko data) on days 3 and 7 pi, compared to wt mice. Unlike wt iBALF, caspase-3/7 activity was not increased upon TR-AM treatment with Tnfsf14-- iBALF (Figure 5E). No differences could be detected in viral titers on day 3 pi (peak of viral replication in this model (28), Supplemental Figure 5K) or in the amount of epithelial (EpcAM+), endothelial (CD31+), and mesenchymal cells (MC, Supplemental Figure 5, L-N). With the exception of neutrophils, which presented higher numbers in *Tnfsf14*-/- mice on day 3 pi but not at later time points (Supplemental Figure 50), no differences could be shown for other BALF leukocyte populations (Supplemental Figure 5, P-S). This data suggested that TNFSF14-associated cell death was confined to the TR-AM compartment. Alongside, absence of the ligand resulted in decreased weight loss, hinting at a beneficial effect of TNFSF14 blockade (Figure 5F). Aiming at a therapeutic approach, we used a neutralizing anti-TNFSF14 antibody (11) and observed higher BALF and lung tissue TR-AM numbers on day 7 pi (Figure 5, G-H), an attenuated weight loss in the anti-TNFSF14 group (Figure 5I), and confirmed lower caspase-3 activity in TR-AMs after ex vivo iBALF treatment (Figure 5J), highlighting TNFSF14 as the driver of post-influenza TR-AM death.

213

214

215

216

212

191

192

193

194

195

196

197

198

199

200

201

202

203

204

205

206

207

208

209

210

211

TNFSF14 is released by neutrophils during the acute IAV infection phase

To identify the cellular source of TNFSF14 during IAV pneumonia, we analyzed expression of the transmembrane form of TNFSF14 on leukocytes (CD45⁺ cells),

epithelial cells, MC, and endothelial cells in the lungs of mock- and IAV-infected mice on day 7 pi. TNFSF14 expression was significantly increased in epithelial cells and leukocytes (Figure 6A). This was in accordance with our IHC data, which revealed a prominent signal increase within the leukocyte-infiltrated interstitium and alveolar space on day 7 pi (Figure 6B). Soluble TNFSF14 was detected in the serum of infected mice as early as day 3 pi, further suggesting that blood-derived immune cells contributed to the increase in TNFSF14 levels within the lung (Figure 6C). Single cell (sc)RNA-Seg analysis of pre-gated CD45+ cells from whole lung digests on days 3 and 7 pi revealed a total of 14 immune cell clusters on day 3 pi, including TR-AMs, BMDM, interstitial macrophages (IM), B and T cells, conventional dendritic cells (cDCs), plasmacytoid DCs (pDCs), monocyte-derived DCs (moDCs), NK cells, three monocyte clusters with different gene signatures: monocytes 1 (Ccr2, Ly6a2, F13a1, Mgst1, Aldh2), monocytes 2 (Tgfb1, Sirpb1c, Otulin1, Plcg2, Zfp710), and monocytes 3 (Eno3, Cd300e, Agpat4, Rbpms, Slc12a2), and two neutrophil clusters: neutrophils 1 (Ier5, Ier3, Smox, Gm8995, Ccrl2) and neutrophils 2 (Picalm, Jund, Hmgb2, Map1lc3b, Slc2a3). Eleven clusters were identified on day 7 pi, including TR-AMs, BMDM, IM, B cells, CD4+, CD8+, proliferating T cells, pDCs, cDCs, NK cells, and neutrophils (Figure 6, D-E). On both time points, neutrophils were revealed as the main leukocyte population expressing *Tnfsf14*, with a minor contribution from NK and T cells. Ltbr gene expression was higher than Tnfrsf14 in all monocyte/macrophage populations, including TR-AMs (Figure 6, D-E). qPCR analysis revealed an upregulation of *Tnfsf14* in neutrophils isolated from peripheral blood on day 2 pi, (Figure 6F), recapitulated in BALF neutrophils of patients with IAV ARDS (Figure 6G). Flow cytometry analysis confirmed neutrophils as the main TNFSF14-expressing leukocyte population on day 3 pi, with no ligand expression on bone marrow-derived neutrophils from non-infected mice (Figure 6H). Both soluble and transmembrane

217

218

219

220

221

222

223

224

225

226

227

228

229

230

231

232

233

234

235

236

237

238

239

240

241

TNFSF14 were revealed to contribute to TR-AM apoptosis, as iBALF treatment of day 3 TR-AMs led to a significant increase in caspase3-/7 activity, comparable to the increase induced by TR-AM co-culture with day 3 neutrophils, even at the presence of a metalloproteinase inhibitor preventing TNFSF14 shedding (Supplemental Figure 6A) (29). We then tested whether neutrophil depletion via i.p. administration of an anti-Ly6G antibody (30) would improve post-influenza TR-AM survival. Following successful neutrophil depletion (Supplemental Figure 6, B-E), mice demonstrated an attenuated weight loss up to day 7 pi (Supplemental Figure 6F), which was in accordance with previously published data (31, 32). Neutrophil-depleted mice presented lower TNFSF14 levels (Figure 6, I-J), compared to the isotype-treated group, with higher BALF and lung-tissue TR-AM numbers on day 7 pi (Figure 6, K-L). No significant differences in other BALF immune cells could be observed (Supplemental Figure 6, G-K), demonstrating the depletion specificity of the anti-Ly6G antibody.

Outcome of post-influenza pneumococcal pneumonia is improved by targeting

the TNFSF14 ligand-receptor axis

Having established that TR-AM loss was driven by the TNFSF14-LTbR axis in severe IAV infection, we tested whether TR-AM preservation would improve co-infection outcome (Figure 1, A-D). Indeed, *Tnfsf14*-/- mice showed significantly improved survival and reduced weight loss (Figure 7, A-B), and reduced BALF pneumococcal burden on day 9 pi/48h post-Spn (Figure 7, C-D), whereas no difference could be shown for spleen bacterial burden (Supplemental Figure 7A). Despite a massive neutrophil influx in both groups (Supplemental Figure 7B), *Tnfsf14*-/- mice maintained TR-AMs (Figure 7E). No significant differences could be observed in the phagocytosis capacity and the percentage of phagocytic TR-AMs on day 7 pi, the time point of pneumococcal infection

(Supplemental Figure 7, C-D). Based on the lack of difference in overall phagocytic capacity, we concluded that the improved bacterial clearance in *Tnfsf14-/-* mice was mainly attributed to the higher number of surviving TR-AMs. Treatment with the neutralizing anti-TNFSF14 antibody led to a similar improvement in survival and weight loss (Figure 7, F-G), supporting the hypothesis that post-influenza TR-AM maintenance was key to survive secondary pneumococcal infection. Finally, we performed orthotopic transfer of wt, Tnfrsf14-/-, or Ltbr/- TR-AMs in co-infected mice (schematics in Figure 7H). Pneumococcal superinfection proved lethal in mice that received no cells or *Tnfrsf14*-/- TR-AMs, whereas transfer of *Ltbr*-/- TR-AMs rescued 75% of mice (Figure 7I). Transfer of wt TR-AMs only slightly increased survival, indicating that transferred wt TR-AMs experienced TNFSF14-dependent apoptosis after transfer on day 3 pi. Ltbr/-TR-AMs additionally showed a superior phagocytosis capacity for Spn compared to wt TR-AMs when infected ex vivo (Figure 7J), which may have additionally contributed to the improved survival observed in the Ltbr/- TR-AM recipient group. Based on these results, we conclude that targeting the TNFSF14 signaling axis could revert TR-AM death in the aftermath of severe IAV-induced lung injury and thus prevent the transition to secondary bacterial pneumonia (Figure 7K).

269

270

271

272

273

274

275

276

277

278

279

280

281

282

283

284

285

Discussion

287

288

289

290

291

292

293

294

295

296

297

298

299

300

301

302

303

304

305

306

307

308

309

310

311

312

Lower respiratory tract infections (LRTIs) are a leading global cause of death, with IAV infection playing a major role due to a variety of potential complications, most notably secondary bacterial infections, which greatly increase the risk of respiratory failure and ICU admission, and overall mortality (21, 33, 34). With no causative pharmacological treatment for pneumonia-related lung injury, research has focused on understanding the mechanisms behind severe IAV pneumonia and the transition to post-influenza secondary infection. Proposed mechanisms include bacterial dissemination due to IAV-associated epithelial cell death, fibrin deposition, impaired mechanical clearance, microbial dysbiosis, and interferon-driven suppression of phagocyte function (2, 35, 36). As the lungs' first line of defense, IAV-induced TR-AM depletion is a critical step in compromising host immunity. Patient and animal studies have demonstrated that severe viral infections drive TR-AM depletion and niche replenishment by BMDM, with the depletion phase aligning with peak susceptibility to bacterial infection (3, 37-39), yet the involved pathways remain poorly understood. Here, we identified TNFSF14 as a driver of TR-AM loss during IAV pneumonia. In the first week post-infection, TR-AM numbers progressively declined, while other leukocytes gradually entered the alveoli in response to viral infection. TR-AM fate after acute infection is dictated by cell death-inducing mechanisms, impaired self-renewal capacity, and loss of pro-survival signals from the injured neighboring epithelium (6, 7). The extent of TR-AM depletion and the intensity of the inflammatory response shape the composition and (re)programming of lung-resident cells after infection (40). Our own previous data indicates that partial TR-AM loss enables the recruitment of circulating BMDM, which are essential for post-viral repair through their transitioning into pro-homeostatic phenotypes (41). Co-existence of newly recruited BMDM and surviving original TR-AMs is the outcome of a balanced immune response, which

culminates in BMDM-orchestrated tissue repair and return to homeostasis, assisted by the tolerogenic functions of TR-AMs, aimed at restricting epithelial damage (42, 43). Infection severity determines the extent of TR-AM depletion, with a dramatic loss upon severe IAV pneumonia, as demonstrated in our model. Recruitment of proinflammatory immune cells and chemokine abundance contribute to viral clearance, but can also escalate to a dysbalanced immune response (44). The highly proinflammatory programming of BMDM can aggravate local injury and promote aberrant lung remodeling (18, 28), while dysregulated neutrophil migration and activation positively correlate with disease severity and poor patient outcomes (45, 46). Following TR-AM depletion, early recruitment of professional phagocytes such as BMDM and neutrophils failed to control bacterial spread, leading to dramatic bacterial outgrowth within 24h of Spn infection. This aligns with prior studies demonstrating high susceptibility to secondary pneumococcal infection 5-7 days after IAV infection, coinciding with the TR-AM depletion phase (3). IFN-y, which is profusely released in the alveoli as part of the antiviral response, heavily impairs TR-AM antibacterial properties, as it downregulates the macrophage receptor with collagenous structure scavenger receptor (MARCO) on TR-AM surface, one of the key elements in TR-AM antibacterial response (47, 48). Defective chemokine production by macrophages, as observed in severe IAV infection and sepsis models, further aggravates disease outcome (49, 50). The near-complete TR-AM loss within a microenvironment of exuberant death-inducing signals in our model highlights an additional important step towards the establishment of lethal post-viral pneumococcal pneumonia. Though a considerable advantage in terms of antibacterial properties has been described for infection-experienced BMDM and newly originating, BMDM-derived, TR-AMs after IAV infection (19), pneumococcal infection in that model was performed weeks after the initial viral hit, as opposed to the window of increased host vulnerability during the acute

313

314

315

316

317

318

319

320

321

322

323

324

325

326

327

328

329

330

331

332

333

334

335

336

337

infection phase described in our study. At this point, TR-AMs showed superior phagocytic capacity and similar killing capacity to BMDM. Thus, preserving TR-AMs early on, may provide critical protection until re-establishment of a fully functional resident macrophage niche, including infection-trained BMDM, has been completed. The remarkable TR-AM loss in C57BL/6 wild-type mice in our study differs from previously published data, where mouse genetic strain determined TR-AM survival. with BALB/c mice exhibiting a drastic TR-AM reduction, as opposed to C57BL/6 mice, which maintained TR-AMs of an altered phenotype (51). In this study by Califano et al., a relatively low dose of IAV PR8 was administered intranasally, whereas we administered a high viral dose orotracheally, aiming at inducing severe pneumonia. Animal strain and administration route for the infection may, therefore, depict a limitation of our study, as results may differ for different in vivo models. Transcriptomic and flow cytometry analyses revealed apoptosis as the primary cause of post-influenza TR-AM death, largely independent of direct viral infection, suggesting the involvement of a death-inducing ligand. While apoptosis promotes early viral spread (22, 52), it also limits infection through elimination of infected cells (53, 54). Leukocyte- and virus-driven alveolar epithelial cell apoptosis, however, compromises the gas-blood barrier and impairs gas exchange (25, 28). Apoptosis inhibition can, therefore, influence infection outcome. To compensate for any effect of caspase inhibition on early virus propagation, we began our treatment on day 2 pi and observed no significant difference in viral titers on day 3 pi, the peak of viral replication in this model (28). Caspase-8 inhibition was chosen based on our in vitro data, which showed a clear advantage over caspase-3 inhibition after TR-AM iBALF treatment. This initially surprising result could be potentially explained through PANoptosis as the joint result of pyroptosis, apoptosis, and necroptosis. This would permit cell death via caspase-3independent apoptosis or pyroptosis. Caspase-8 is involved in both these pathways

339

340

341

342

343

344

345

346

347

348

349

350

351

352

353

354

355

356

357

358

359

360

361

362

363

(55-58) and is currently the only known programmed cell death (PCD) member that connects all PCD pathways. This can explain the complete abrogation of TR-AM death on day 3 pi, the reduced weight loss, and the improved TR-AM survival upon caspase-8 inhibition. Nevertheless, the PANoptosis concept suggests that a single PCD component cannot individually rescue cells once PANoptosis has been initiated, which might explain why TR-AM loss was not completely prevented on day 7 pi, when deathinducing signals are highly abundant (59-61). Stochastic interrogation of TNFSF members revealed significant upregulation of TNFSF14 in infected mouse lungs, with high soluble TNFSF14 levels also found in BALF from patients with severe virus-induced ARDS. Previous studies on severe viral pneumonia and sepsis positively linked elevated BALF/serum TNFSF14 levels to disease severity (15, 16, 62, 63). Depending on cell type, pathogen interaction, and receptor availability, TNFSF14 can influence cell survival, profile (re)programming, immune response establishment, and infection memory (10, 64). TNFSF14 has been previously described as a determinant of macrophage survival, phenotype, and antibacterial properties (65-67), however, extensive studies regarding post-influenza TR-AM death are lacking. In our study, TNFSF14 deletion or blockade preserved TR-AMs and improved survival and weight loss during co-infection. These benefits were not solely due to reduced bacterial burden but likely stemmed from enhanced tissue repair and accelerated return to homeostasis due to improved TR-AM survival. Previous work from our lab has highlighted TR-AMs as drivers of epithelial repair (41) and mitigators of lung inflammation, even at the cost of bacterial clearance (43). Further experiments would be required to fully address the role of TNFSF14 on pathogen resistance and tolerance in the context of co-infection beyond the lungconfined effect on TR-AM survival.

365

366

367

368

369

370

371

372

373

374

375

376

377

378

379

380

381

382

383

384

385

386

387

388

Post-influenza TNFSF14-induced TR-AM death was cell-specific, with no significant differences in other leukocytes (except neutrophils on day 3 pi) or in endothelial, mesenchymal, or epithelial cells between wt and *Tnfsf14*^{-/-}mice. TNFSF14 treatment did not worsen virus-induced death in alveolar epithelial cells, suggesting TNFSF14 is not a strong driver of post-influenza distal epithelial cell apoptosis. We identified neutrophils as the main leukocyte source of TNFSF14, which is in accordance with previously published data (68, 69). TNFSF14 has been shown to play an instrumental role in NK and T cell activation and expansion (11, 17, 70) and DC maturation (71) and may thus serve as an intermediate between the acute and adaptive immune response. Aberrant release due to dysregulated neutrophil activation could offer an alternative explanation for the abundant TNFSF14 presence upon severe infection. This is in accordance with literature, as high circulating or organ-specific TNFSF14 levels have been positively correlated with highly inflammatory states (13, 15, 72-74) and blocking of the ligand was shown to limit inflammation and attenuate organ injury (75). TNFRSF14 and LTbR, the two competitor TNFSF14 receptors, followed distinct kinetics in terms of transcriptional regulation and protein expression in TR-AMs during the infection course. Attenuated TR-AM loss after IAV infection of Ltbr/- mice, compared to Tnfrsf14-/- mice, and improved survival after intrapulmonary transfer of Ltbr/-TR-AMs to co-infected wt mice, demonstrated a stronger impact on TR-AM death for LTbR. Given the more prominent TR-AM preservation in *Tnfsf14*-/- mice compared to Ltbr/-mice, we hypothesize that cell death could also be initiated through ligation of TNFSF14 to TNFRSF14, potentially through activation of a co-receptor, as TNFRSF14 lacks a pro-death domain (10, 76). It should be noted, however, that engagement of LTbR by TNFSF14 on macrophages is not merely confined to apoptosis induction. Transforming growth factor-beta (TGF-β) can be secreted upon crosslinking (77), which has been shown to drive an immunoparalysis state in the aftermath of infection,

390

391

392

393

394

395

396

397

398

399

400

401

402

403

404

405

406

407

408

409

410

411

412

413

414

further enhancing secondary infection susceptibility (78). LTbR-TNFSF14 interaction on the endothelium alters microvasculature structure, which can in turn favor the recruitment of immune cells (79). The intricate nature of TNFSF14-TNFRSF14/LTbR interactions thus points at a multitude of potential roles for the signaling axis in the context of influenza, besides TR-AM depletion. Nevertheless, with clinical trials in the context of virus-induced pneumonia and systemic inflammation already revealing beneficial safety profiles (63, 80, 81), therapeutic interventions disrupting TNFSF14-initiated intercellular pathways to preserve TR-AM function appear as promising approaches for improving host defense in the context of IAV pneumonia.

426 **Methods**

427 Sex as a biological variable. Sex was not considered as a biological variable for patient samples. Both male and female mice were used for all studies. 428 429 Mice. Wt C57BL/6 mice were purchased from Charles River Laboratories. Tnfsf14-/-430 (82), Tnfrsf14-/- (83), and Ltbr/- (84) mice were a gift from Prof. Klaus Pfeffer (Heinrich 431 Heine University Düsseldorf, Düsseldorf, Germany). Trisf10-/- (85) mice were obtained 432 from AMGen. All mice were bred under specific-pathogen-free conditions (SPF) and 433 infected at 10-12 weeks of age. In vivo infection. For in vivo IAV infection experiments, mice were orotracheally 434 435 inoculated with 250-1000ffu of A/Puerto Rico/8/1934 (PR8, H1N1) influenza virus. Control groups were inoculated with sterile PBS^{-/-}. For co-infection experiments, mice 436 437 were i.n. infected with 20cfu Spn [serotype 3, strain PN36 (NCTC 7978), provided by 438 the group of M. Witzenrath, Department of Infectious Diseases and Pulmonary 439 Medicine, Charité, University Medicine Berlin, Berlin, Germany] 7 days after IAV 440 infection. 441 In vivo treatment. For apoptosis inhibition, wt mice were infected with 500ffu (day 7 experiments) or 1000ffu IAV (day 3 experiments) and treated with s.c. injections of 442 443 10mg/kg of a specific caspase-8 inhibitor (Z-IETD-FMK, R&D Systems), or a DMSO 444 control. For day 3 experiments, treatment involved a single injection on day 2 pi, 445 whereas daily injections were applied days 2-6 pi for analysis on day 7 pi. Neutrophil depletion was performed through the i.p. application of 200µg anti-1A8 antibody 446 447 (InVivoPlus rat anti-mouse Ly6G, cat. BP0075-1, BioXCell) or an anti-2A3 isotype control (InVivoPlus™ rat IgG2a isotype control, anti-trinitrophenol, cat. BP0089, 448 449 BioXCell) diluted in sterile PBS in mice infected with 500ffu IAV on days -1, 1, 3, and 450 5 pi. TNFSF14 neutralization was achieved with a mouse anti-mouse LIGHT blocking antibody (clone 3D11, IgG2b, k, isotype control mouse IgG2b, clone 27-35, 451

452 BioLegend), kindly provided by Prof. José Ignacio Rodríguez Barbosa and Prof. Maria-453 Luisa del Rio (INBIOMIC, University of León, León, Spain). A single i.p. injection of 454 500µg of antibody or isotype control was performed two days after IAV infection with 455 500ffu. For in vivo treatment with rTNFSF14, 10µg of carrier-free mouse rTNFSF14 (cat. 1794-LT, R&D Systems) diluted in 0.03mL PBS-/- were orotracheally administered 456 457 to IAV-infected mice on days 1 and 2 pi for analysis on day 3 pi. Adoptive TR-AM transfer. Murine TR-AM were obtained from the BALF of naïve wt, 458 459 Tnfrsf14^{-/-}, and Ltbr^{-/-} mice, as previously described (25). Adoptive transfer of 400,000 TR-AM per mouse was performed on day 3 after infection of wt mice with 250ffu IAV, 460 461 with an engraftment efficiency of 14-20% calculated 24h later, at a time point where over 70% of the original TR-AM pool was still detectable in the BALF of infected mice 462 463 (data not shown). Secondary pneumococcal infection was performed four days later. 464 TR-AM isolation and cell culture for ex vivo treatment. Following BALF extraction from naïve mice, cells were resuspended in full TR-AM medium (RPMI-1640/2% fetal 465 466 bovine serum (FBS)/2.5% HEPES/1% L-glutamine/1% penicillin/streptomycin). TR-467 AMs were seeded at a density of 10-50,000 cells/well on a 96-well plate. Colorimetric viability assay for ex vivo treated TR-AMs. Primary TR-AMs isolated from 468 469 the BALF of naïve wt mice and BALF TR-AMs from control patients who underwent 470 routine bronchoscopy for diagnostic purposes and revealed normal BALF cellularity 471 were treated with 0.1mL TR-AM medium containing 10% iBALF or rTNFSF14 for 24h. For caspase inhibition experiments, cells were pre-incubated in 50µM of a specific 472 473 caspase-3 (Z-DEVD-FMK, cat. FMK004, R&D Systems) or caspase-8 inhibitor (Z-IETD-FMK, cat. FMK007, R&D Systems) for 3h prior to BALF treatment. Viability was 474 475 assessed via colorimetric assay (Cell Counting Kit-8, cat. 96992, Sigma Aldrich), as 476 per the manufacturer's instructions, and was considered proportional to the measured light absorbance. Absorbance was measured in an iMark microplate reader (Bio-Rad). 477

Caspase-3/7 and caspase-8 activity. Wt, Tnfrsf14-/-, and Ltbr/- BALF TR-AMs were treated with 0.1mL TR-AM medium containing 10% day 0 or day 7 iBALF from wt or Tnfsf14-- mice for 24h. Lyophilized Caspase-Glo[®] 3/7 or Caspase-Glo[®] 8 substrate (Promega) was resuspended in 10mL luciferase-containing Caspase-Glo® buffer (Promega) and added a 0.1mL/well to the cells. After 1h incubation at RT, cells were transferred to a black 96-well plate for luminescence detection using a 520/25 filter in an FLx800 fluorescence reader (BioTek Instruments). For ligand blocking experiments, iBALF had been previously incubated with 1µg/mL of the mouse anti-mouse TNFSF14 antibody or an isotype control for 1h at 4°C prior to iBALF treatment. For TNFSF14 receptor blocking experiments, TR-AMs were pretreated with 1µg/mL for 1h at 37°C, CO₂, prior to iBALF treatment, to achieve receptor saturation. Antibodies included Armenian hamster anti-mouse anti-TNFRSF14 (CD270 (HVEM) monoclonal antibody, LH1, functional grade, cat. 16-5962-85, eBioscienceTM), Armenian hamster anti-mouse isotype control (cat. 16-4888-85, eBioscienceTM), rat anti-mouse anti-LTbR (clone 4H8-WH2, developed by the laboratory of Dr. Carl F. Ware, marketed by AdipoGen Life Sciences, and kindly provided by Prof. José Ignacio Rodríguez Barbosa and Prof. Maria-Luisa del Rio, University of León, Spain), and rat anti-mouse IgG2a isotype control (cat. AG-35B-0002-C050, AdipoGen). To dissect the roles of soluble and transmembrane TNFSF14 on TR-AM apoptosis, flow-sorted day 3 TR-AMs were either treated with iBALF or co-cultured with neutrophils at a 1:5 ratio for 24h. Marimastat (cat. M2699, Sigma-Aldrich) was added at a concentration of 10µM to prevent TNFSF14 shedding. Spn load after in vivo infection. Two days after IAV infection and 6-72h after Spn infection, BALF, lungs, and spleens from co-infected mice were harvested and homogenized. A series of inoculum dilutions in NaCl was prepared for each sample in 1:10 dilution steps. For each dilution step, 4 x 0.01mL inoculum were pipetted on a

478

479

480

481

482

483

484

485

486

487

488

489

490

491

492

493

494

495

496

497

498

499

500

501

502

504 blood agar plate and stored at 37°C overnight. Bacterial load was calculated by counting the average number of separately grown colonies, multiplied by 10^{number of} 505 dilution step*100 (= number of colonies in 1mL). 506 Ex vivo phagocytosis and killing assay. Wt and Ltbr/- naïve BALF TR-AMs were 507 508 isolated as previously described. Cells were seeded a 100,000 cells/well on a 96-well 509 round-bottom plate and ex vivo infected with Spn at an multiplicity of infection (MOI) 510 1000 for 10min (37°C). Cells were vigorously washed 5 times in ice-cold PBS to 511 remove any extracellular bacteria and lysed in water. An inoculum dilution series of cell 512 lysates was pipetted on blood agar plates as described above. Total colony count on 513 the following day depicted phagocytosed bacteria. For flow cytometry-based 514 comparison of day 8 TR-AMs and BMDM Spn uptake and killing, 100,000 cells of whole 515 BALF cell samples were ex vivo infected with Spn at an MOI 100 for 10min (t0). Cells 516 were washed three times with ice-cold PBS and were either fixed and permeabilized 517 using the eBioscience™ Foxp3/Transcription Factor Staining Buffer Set (cat. 00-5523-518 00, Invitrogen), as per the manufacturer's instructions, or returned to the incubator for 519 an additional 30min (t1) in sterile medium, after which the same procedure was performed. Staining was performed in two steps, starting with an anti-Spn antibody 520 (rabbit, cat. PA17259, Invitrogen) or a rabbit IgG isotype control (cat. ab172730, 521 522 abcam) at a concentration of 40µg/mL for 1h at RT, followed by leukocyte surface 523 staining containing a secondary donkey anti-rabbit IgG (H+L) Alexa Fluor™ 555 524 antibody (cat. A-31572, Invitrogen). Non-infected samples were used 525 autofluorescence controls. Phagocytosis capacity was reflected in the percentage of Spn+ cells at (t0), killing capacity at (t1) was determined for each macrophage 526 population as follows: percent killing = 100 - [(%Spn+ cells at t1/%Spn+ cells at t0) × 527 528 100].

RT² Profiler PCR Arrays. RT² profiler PCR arrays (Qiagen) were used for pathway or group gene expression analysis of flow-sorted TR-AMs. RNA isolation, genomic DNA elimination, reverse transcription, cDNA synthesis, and qPCR were performed according to the manufacturer's instructions. In samples with low RNA amount (<1µg), a pre-amplification of cDNA targets preceded qPCR by addition of a PCR master mix (RT2 PreAMP PCR Mastermix, Qiagen) and a species- and pathway-specific primer mix (PBM-063Z-RT² PreAMP cDNA Synthesis Primer Mix for Mouse TNF Ligands and Receptors, PBM-212Z - RT² PreAMP cDNA Synthesis Primer Mix for Mouse Cell Death PathwayFinder[™], cat.330241, Qiagen) to the cDNA samples. PCR components were added to the 96-well plate format provided by the company (PAMM-063ZC-24-RT² Profiler™ PCR Array Mouse TNF Signaling Pathway, PAMM-212ZC-12-RT² Profiler™ PCR Array Mouse Cell Death PathwayFinder, cat. 330231, Qiagen). Realtime PCR was performed in the StepOnePlus™ Real-Time PCR System and in the QuantStudio[™] 3 Real-Time PCR System (Applied Biosystems[™]). Data analysis was performed with the company's web-based data analysis software (GeneGlobe Data Analysis Center, Qiagen). A detailed description of the data statistical interpretation can be found in the 'Supplemental methods' document. Single-cell RNA sequencing. To identify the main leukocyte TNFSF14 source, 500,000 live leukocytes (gated as Sytox- CD45+) from the homogenized single-cell lung suspensions of IAV-infected mice on day 3 and 7pi were sorted into 0.35µL 0.04% BSA/PBS-/-. Following viability control, 10,000 cells were loaded onto Chromium Chip B (10X Genomics). Gel beads in emulsion (GEM) generation, cDNA synthesis and amplification, and library preparation were performed with the Chromium Single Cell 3' Reagent Kit v3.1 (10X Genomics), as per the manufacturer's protocol. Indexed libraries were sequenced on an Illumina NextSeg2000. Prior to analysis, reads were aligned against the mouse genome (GRCm38.p6) and quantified using StarSolo

529

530

531

532

533

534

535

536

537

538

539

540

541

542

543

544

545

546

547

548

549

550

551

552

553

(https://github.com/alexdobin/STAR). Analysis was conducted with the Scanpy software (https://github.com/theislab/scanpy). After quality filtering, raw cell counts were normalized to the median count over all cells and transformed into log space for variance stabilization. Principal component analysis (PCA) identified 14 and 11 components on days 3 and 7 pi, respectively. Uniform Manifold Approximation and Projection (UMAP) embedding was created to identify cell type clusters through Leiden clustering. Doublet analysis was conducted on day 7 using (https://github.com/swolock/scrublet), leading to the removal of a doublet cluster (118 cells). Statistics. Data are shown in scatterplots as single data points. Means ± SEM per group are indicated by bars and error bars. Statistical significance between two groups was calculated using 2-tailed Student's t-test. For comparison between more than two groups, significance was determined by 1-way ANOVA, 2-way ANOVA with Tukey's posthoc test, or by Kruskal-Wallis test followed by Dunn's post hoc comparison test. Survival curves were compared by log-rank (Mantel-Cox) test. P<0.05 was considered as significant. *P < 0.05; **P < 0.01; ***P < 0.005. Graphs were prepared using GraphPad Prism (GraphPad Software version 10.2.3). Study approval. Animal experiments were approved by the regional authorities of the State of Hesse (Regierungspraesidium Giessen, Germany) and by the Institutional Ethics Committee at the IBioBA Institute (Buenos Aires, Argentina). Use of human BALF samples was approved by the University of Giessen Ethics Committee, samples were provided by the biobank of the German Center for Lung Research (DZL). Written informed consent was received prior to sample use. Data availability. Data supporting the findings of this study are available within the article and its supplemental material. Values for all data points in graphs are reported in the Supporting Data Values file. ScRNA-Seq data can be accessed under the GEO

555

556

557

558

559

560

561

562

563

564

565

566

567

568

569

570

571

572

573

574

575

576

577

578

579

582 (https://www.ncbi.nlm.nih.gov/geo/query/acc.cgi?acc=GSE273805).

Author contributions

CM, CP, MRF, KF, KK, CYW, JB, ME designed and performed experiments, evaluated, and interpreted data. CM wrote the manuscript. AIVA and SH designed, performed, and interpreted scRNA-Seq experiments. IA performed imaging analysis. HS, SG, ML performed sequencing and bioinformatics analyses. JH and ADG performed immunohistochemistry analysis. KP provided genetically modified mice. MLDR and JIRB provided the neutralizing anti-TNFSF14 and anti-LTbR antibodies. IV performed bronchoscopy for the acquisition of human BALF samples. CP, SG, ML, ADG, IV, UM, and SH revised the manuscript. SH conceived the scientific question, designed experiments, interpreted data, and financed the study.

Acknowledgements

This work was supported by the German Research Foundation (Deutsche Forschungsgemeinschaft, DFG) under following projects: KFO309 project P2/P9, project number 284237345; SFB-TR84 project number 114933180; SFB1021 project number 197785619; the Cardiopulmonary Institute (CPI; DFG EXC 2026 project number 390649896), and by the State of Hesse: LOEWE grant 'diffusible signals' project number LOEWE/2/13/519/03/06.001(0002)/74, LOEWE professorship, funding line 4a, project ID III L7–519/05.00.002. We would like to thank Martin Witzenrath and Birgit Gutbier for providing us with the serotype 3 Spn bacterial strain. We would like to thank Maria Gross, Stefanie Jarmer, Larissa Hamann, Florian Lück, Julia Stark, and Josephine Guth, for excellent technical support. Experimental layout schematics and summary figure were created with BioRender.com.

References

- 608 1. Qiao M, et al. The prevalence of influenza bacterial co-infection and its role in
- disease severity: A systematic review and meta-analysis. J Glob Health.
- 610 2023;13:04063.
- 611 2. McCullers JA. The co-pathogenesis of influenza viruses with bacteria in the
- 612 lung. Nat Rev Microbiol. 2014;12(4):252-62.
- 613 3. Ghoneim HE, et al. Depletion of alveolar macrophages during influenza
- infection facilitates bacterial superinfections. *J Immunol.* 2013;191(3):1250-9.
- 615 4. Malainou C, et al. Alveolar macrophages in tissue homeostasis, inflammation,
- and infection: evolving concepts of therapeutic targeting. J Clin Invest.
- 617 2023;133(19).
- 5. Wang J, et al. Innate immune response of human alveolar macrophages during
- influenza A infection. *PLoS One.* 2012;7(3):e29879.
- 620 6. Bain CC, and MacDonald AS. The impact of the lung environment on
- macrophage development, activation and function: diversity in the face of
- 622 adversity. *Mucosal Immunol.* 2022;15(2):223-34.
- 623 7. Aegerter H, et al. Biology of lung macrophages in health and disease. *Immunity*.
- 624 2022;55(9):1564-80.
- 625 8. Cardani A, et al. Alveolar Macrophages Prevent Lethal Influenza Pneumonia By
- Inhibiting Infection Of Type-1 Alveolar Epithelial Cells. PLoS pathogens.
- 627 2017;13(1):e1006140.
- 9. Purnama C, et al. Transient ablation of alveolar macrophages leads to massive
- pathology of influenza infection without affecting cellular adaptive immunity.
- European journal of immunology. 2014;44(7):2003-12.

- 631 10. Ward-Kavanagh LK, et al. The TNF Receptor Superfamily in Co-stimulating and
- 632 Co-inhibitory Responses. *Immunity*. 2016;44(5):1005-19.
- 633 11. del Rio ML, et al. Immunotherapeutic targeting of LIGHT/LTbetaR/HVEM
- pathway fully recapitulates the reduced cytotoxic phenotype of LIGHT-deficient
- 635 T cells. *MAbs.* 2016;8(3):478-90.
- 636 12. Otterdal K, et al. Platelet-derived LIGHT induces inflammatory responses in
- endothelial cells and monocytes. *Blood.* 2006;108(3):928-35.
- 638 13. Mehta AK, et al. Tumor necrosis factor family member LIGHT acts with IL-1beta
- and TGF-beta to promote airway remodeling during rhinovirus infection. *Allergy*.
- 640 2018;73(7):1415-24.
- 14. Doherty TA, et al. The tumor necrosis factor family member LIGHT is a target
- for asthmatic airway remodeling. *Nature medicine*. 2011;17(5):596-603.
- 643 15. Arunachalam PS, et al. Systems biological assessment of immunity to mild
- versus severe COVID-19 infection in humans. Science. 2020;369(6508):1210-
- 645 20.
- 646 16. Perlin DS, et al. Levels of the TNF-Related Cytokine LIGHT Increase in
- Hospitalized COVID-19 Patients with Cytokine Release Syndrome and ARDS.
- 648 *mSphere*. 2020;5(4).
- 649 17. Seo GY, et al. LIGHT-HVEM Signaling in Innate Lymphoid Cell Subsets
- Protects Against Enteric Bacterial Infection. *Cell Host Microbe*. 2018;24(2):249-
- 651 60 e4.
- 652 18. Ellis GT, et al. TRAIL+ monocytes and monocyte-related cells cause lung
- damage and thereby increase susceptibility to influenza-Streptococcus
- 654 pneumoniae coinfection. *EMBO Rep.* 2015;16(9):1203-18.
- 655 19. Aegerter H, et al. Influenza-induced monocyte-derived alveolar macrophages
- confer prolonged antibacterial protection. *Nat Immunol.* 2020;21(2):145-57.

- 657 20. Westphalen K, et al. Sessile alveolar macrophages communicate with alveolar
- epithelium to modulate immunity. *Nature.* 2014;506(7489):503-6.
- 659 21. Peteranderl C, et al. Human Influenza Virus Infections. Semin Respir Crit Care
- 660 *Med.* 2016;37(4):487-500.
- Herold S, et al. Apoptosis signaling in influenza virus propagation, innate host
- defense, and lung injury. *J Leukoc Biol.* 2012;92(1):75-82.
- 23. D'Arcy MS. Cell death: a review of the major forms of apoptosis, necrosis and
- autophagy. Cell Biol Int. 2019;43(6):582-92.
- Orning P, and Lien E. Multiple roles of caspase-8 in cell death, inflammation,
- and innate immunity. *J Leukoc Biol.* 2021;109(1):121-41.
- 667 25. Hogner K, et al. Macrophage-expressed IFN-beta contributes to apoptotic
- alveolar epithelial cell injury in severe influenza virus pneumonia. *PLoS Pathog.*
- 669 2013;9(2):e1003188.
- 670 26. Peteranderl C, et al. Macrophage-epithelial paracrine crosstalk inhibits lung
- edema clearance during influenza infection. *J Clin Invest.* 2016;126(4):1566-80.
- 672 27. Skeate JG, et al. TNFSF14: LIGHTing the Way for Effective Cancer
- 673 Immunotherapy. Front Immunol. 2020;11:922.
- 674 28. Herold S, et al. Lung epithelial apoptosis in influenza virus pneumonia: the role
- of macrophage-expressed TNF-related apoptosis-inducing ligand. *J Exp Med.*
- 676 2008;205(13):3065-77.
- 677 29. Celik S, et al. Proinflammatory and prothrombotic effects on human vascular
- 678 endothelial cells of immune-cell-derived LIGHT. Eur J Med Res.
- 679 2009;14(4):147-56.
- 680 30. Davis RWt, et al. Luminol Chemiluminescence Reports Photodynamic Therapy-
- Generated Neutrophil Activity In Vivo and Serves as a Biomarker of Therapeutic
- 682 Efficacy. *Photochem Photobiol.* 2019;95(1):430-8.

- 683 31. Narasaraju T, et al. Excessive neutrophils and neutrophil extracellular traps
- 684 contribute to acute lung injury of influenza pneumonitis. Am J Pathol.
- 685 2011;179(1):199-210.
- 686 32. Reilly EC, et al. The Effects of Acute Neutrophil Depletion on Resolution of
- Acute Influenza Infection, Establishment of Tissue Resident Memory (TRM),
- and Heterosubtypic Immunity. *PLoS One.* 2016;11(10):e0164247.
- 689 33. Okahashi N, et al. Secondary streptococcal infection following influenza.
- 690 *Microbiol Immunol.* 2022;66(6):253-63.
- 691 34. Lim YK, et al. Impact of bacterial and viral coinfection in community-acquired
- 692 pneumonia in adults. *Diagn Microbiol Infect Dis.* 2019;94(1):50-4.
- 693 35. Connolly E, and Hussell T. The Impact of Type 1 Interferons on Alveolar
- Macrophage Tolerance and Implications for Host Susceptibility to Secondary
- Bacterial Pneumonia. *Front Immunol.* 2020;11:495.
- 696 36. McKelvey M, et al. IL-10 Counteracts IFN-gamma to Alleviate Acute Lung Injury
- in a Viral-Bacterial Superinfection Model. Am J Respir Cell Mol Biol.
- 698 2024;71(1):110-20.
- 699 37. Cole SL, et al. M1-like monocytes are a major immunological determinant of
- severity in previously healthy adults with life-threatening influenza. *JCI Insight*.
- 701 2017;2(7):e91868.
- 702 38. Liao M, et al. Single-cell landscape of bronchoalveolar immune cells in patients
- 703 with COVID-19. *Nat Med.* 2020;26(6):842-4.
- 704 39. Smith AM, and Smith AP. A Critical, Nonlinear Threshold Dictates Bacterial
- 705 Invasion and Initial Kinetics During Influenza. *Sci Rep.* 2016;6:38703.
- 706 40. Martin FP, et al. Alveolar Macrophages: Adaptation to Their Anatomic Niche
- during and after Inflammation. *Cells.* 2021;10(10).

- 708 41. Pervizaj-Oruqaj L, et al. Alveolar macrophage-expressed Plet1 is a driver of lung epithelial repair after viral pneumonia. *Nat Commun.* 2024;15(1):87.
- 710 42. Uderhardt S, et al. Resident Macrophages Cloak Tissue Microlesions to Prevent
 711 Neutrophil-Driven Inflammatory Damage. *Cell.* 2019;177(3):541-55 e17.
- Hetter J, Estiri M, et al. Cell type-specific efferocytosis determines functional plasticity of alveolar macrophages. *Sci Immunol.* 2025;10(107):eadl3852.
- 44. Lamichhane PP, and Samarasinghe AE. The Role of Innate Leukocytes during
 Influenza Virus Infection. *J Immunol Res.* 2019;2019:8028725.
- Tang BM, et al. Neutrophils-related host factors associated with severe disease and fatality in patients with influenza infection. *Nat Commun.* 2019;10(1):3422.
- 718 46. Brandes M, et al. A systems analysis identifies a feedforward inflammatory 719 circuit leading to lethal influenza infection. *Cell.* 2013;154(1):197-212.
- 720 47. Sun K, and Metzger DW. Inhibition of pulmonary antibacterial defense by 721 interferon-gamma during recovery from influenza infection. *Nat Med.* 722 2008;14(5):558-64.
- 723 48. Wu M, et al. Immunomodulators targeting MARCO expression improve 724 resistance to postinfluenza bacterial pneumonia. *Am J Physiol Lung Cell Mol* 725 *Physiol.* 2017;313(1):L138-L53.
- 726 49. Shahangian A, et al. Type I IFNs mediate development of postinfluenza bacterial pneumonia in mice. *J Clin Invest.* 2009;119(7):1910-20.
- Deng JC, et al. Sepsis-induced suppression of lung innate immunity is mediated
 by IRAK-M. *J Clin Invest.* 2006;116(9):2532-42.
- 730 51. Califano D, et al. Effects of Influenza on Alveolar Macrophage Viability Are
 731 Dependent on Mouse Genetic Strain. *J Immunol.* 2018;201(1):134-44.
- Wurzer WJ, et al. Caspase 3 activation is essential for efficient influenza virus
 propagation. *EMBO J.* 2003;22(11):2717-28.

- 734 53. Peteranderl C, and Herold S. The Impact of the Interferon/TNF-Related
- 735 Apoptosis-Inducing Ligand Signaling Axis on Disease Progression in
- Respiratory Viral Infection and Beyond. *Front Immunol.* 2017;8:313.
- 737 54. FitzGerald ES, et al. Competitive Cell Death Interactions in Pulmonary Infection:
- Host Modulation Versus Pathogen Manipulation. *Front Immunol.* 2020;11:814.
- 739 55. Bhadra K. A Mini Review on Molecules Inducing Caspase-Independent Cell
- Death: A New Route to Cancer Therapy. *Molecules*. 2022;27(19).
- 56. Sarhan J, et al. Caspase-8 induces cleavage of gasdermin D to elicit pyroptosis
- during Yersinia infection. *Proc Natl Acad Sci U S A.* 2018;115(46):E10888-E97.
- 743 57. Hughes SA, et al. Caspase-8-driven apoptotic and pyroptotic crosstalk causes
- cell death and IL-1beta release in X-linked inhibitor of apoptosis (XIAP)
- 745 deficiency. *EMBO J.* 2023;42(5):e110468.
- 746 58. Pang J, and Vince JE. The role of caspase-8 in inflammatory signalling and
- 747 pyroptotic cell death. Semin Immunol. 2023;70:101832.
- 59. Sauler M, et al. Cell Death in the Lung: The Apoptosis-Necroptosis Axis. *Annu*
- 749 Rev Physiol. 2019;81:375-402.
- 750 60. Gullett JM, et al. It's All in the PAN: Crosstalk, Plasticity, Redundancies,
- Switches, and Interconnectedness Encompassed by PANoptosis Underlying
- the Totality of Cell Death-Associated Biological Effects. *Cells.* 2022;11(9).
- 753 61. Wang Y, and Kanneganti TD. From pyroptosis, apoptosis and necroptosis to
- PANoptosis: A mechanistic compendium of programmed cell death pathways.
- 755 Comput Struct Biotechnol J. 2021;19:4641-57.
- 756 62. Haljasmagi L, et al. Longitudinal proteomic profiling reveals increased early
- inflammation and sustained apoptosis proteins in severe COVID-19. Sci Rep.
- 758 2020;10(1):20533.

- 759 63. Qu HQ, et al. Circulating LIGHT (TNFSF14) and Interleukin-18 Levels in Sepsis-760 Induced Multi-Organ Injuries. *Biomedicines*. 2022;10(2).
- Heo SK, et al. LIGHT (TNFSF14) Increases the Survival and Proliferation of
 Human Bone Marrow-Derived Mesenchymal Stem Cells. *PLoS One.*
- 763 2016;11(11):e0166589.
- 764 65. Petreaca ML, et al. Vascular endothelial growth factor promotes macrophage 765 apoptosis through stimulation of tumor necrosis factor superfamily member 14 766 (TNFSF14/LIGHT). Wound Repair Regen. 2008;16(5):602-14.
- 767 66. Heo SK, et al. LIGHT enhances the bactericidal activity of human monocytes and neutrophils via HVEM. *J Leukoc Biol.* 2006;79(2):330-8.
- 769 67. Yuan X, et al. LIGHT is increased in patients with coronary disease and regulates inflammatory response and lipid metabolism in oxLDL-induced THP
 1 macrophages. *Biochem Biophys Res Commun.* 2017;490(3):732-8.
- 772 68. Conlon TM, et al. Inhibition of LTbetaR signalling activates WNT-induced regeneration in lung. *Nature*. 2020;588(7836):151-6.
- Zhang J, et al. Two waves of pro-inflammatory factors are released during the
 influenza A virus (IAV)-driven pulmonary immunopathogenesis. *PLoS Pathog.* 2020;16(2):e1008334.
- 77. Desai P, et al. The TNF Superfamily Molecule LIGHT Promotes the Generation of Circulating and Lung-Resident Memory CD8 T Cells following an Acute Respiratory Virus Infection. *J Immunol.* 2018;200(8):2894-904.
- 71. Holmes TD, et al. Licensed human natural killer cells aid dendritic cell maturation via TNFSF14/LIGHT. *Proc Natl Acad Sci U S A.*2014;111(52):E5688-96.

- 783 72. Otterdal K, et al. Increased Serum Levels of LIGHT/TNFSF14 in Nonalcoholic
- 784 Fatty Liver Disease: Possible Role in Hepatic Inflammation. Clin Transl
- 785 *Gastroenterol.* 2015;6(7):e95.
- 786 73. Hsu CY, et al. Circulating TNFSF14 (Tumor Necrosis Factor Superfamily 14)
- 787 Predicts Clinical Outcome in Patients With Stable Coronary Artery Disease.
- 788 Arterioscler Thromb Vasc Biol. 2019;39(6):1240-52.
- 789 74. Manresa MC, et al. A Deficiency in the Cytokine TNFSF14/LIGHT Limits
- 790 Inflammation and Remodeling in Murine Eosinophilic Esophagitis. *J Immunol.*
- 791 2022.
- 792 75. Ware CF, et al. Realigning the LIGHT signaling network to control dysregulated
- 793 inflammation. *J Exp Med.* 2022;219(7).
- 794 76. Shui JW, and Kronenberg M. HVEM is a TNF Receptor with Multiple Regulatory
- Roles in the Mucosal Immune System. *Immune Netw.* 2014;14(2):67-72.
- 796 77. Liang QS, et al. Splenectomy improves liver fibrosis via tumor necrosis factor
- superfamily 14 (LIGHT) through the JNK/TGF-beta1 signaling pathway. *Exp Mol*
- 798 *Med.* 2021;53(3):393-406.
- 799 78. Roquilly A, et al. Local Modulation of Antigen-Presenting Cell Development after
- Resolution of Pneumonia Induces Long-Term Susceptibility to Secondary
- 801 Infections. *Immunity*. 2017;47(1):135-47 e5.
- 802 79. Ramachandran M, et al. Tailoring vascular phenotype through AAV therapy
- promotes anti-tumor immunity in glioma. *Cancer Cell.* 2023;41(6):1134-51 e10.
- 804 80. Perlin DS, et al. Randomized, double-blind, controlled trial of human anti-LIGHT
- 805 monoclonal antibody in COVID-19 acute respiratory distress syndrome. *J Clin*
- 806 *Invest.* 2022;132(3).

- 807 81. Zhang M, et al. A Randomized Phase 1 Study to Assess the Safety and
 808 Pharmacokinetics of the Subcutaneously Injected Anti-LIGHT Antibody,
 809 SAR252067. Clin Pharmacol Drug Dev. 2017;6(3):292-301.
- 82. Scheu S, et al. Targeted disruption of LIGHT causes defects in costimulatory T cell activation and reveals cooperation with lymphotoxin beta in mesenteric lymph node genesis. *J Exp Med.* 2002;195(12):1613-24.
- 813 83. Wang Y, et al. The role of herpesvirus entry mediator as a negative regulator of T cell-mediated responses. *J Clin Invest.* 2005;115(3):711-7.
- 815 84. Futterer A, et al. The lymphotoxin beta receptor controls organogenesis and affinity maturation in peripheral lymphoid tissues. *Immunity.* 1998;9(1):59-70.
- 817 85. Cretney E, et al. Increased susceptibility to tumor initiation and metastasis in

 R18 TNF-related apoptosis-inducing ligand-deficient mice. *J Immunol.*R19 2002;168(3):1356-61.

821 Figures

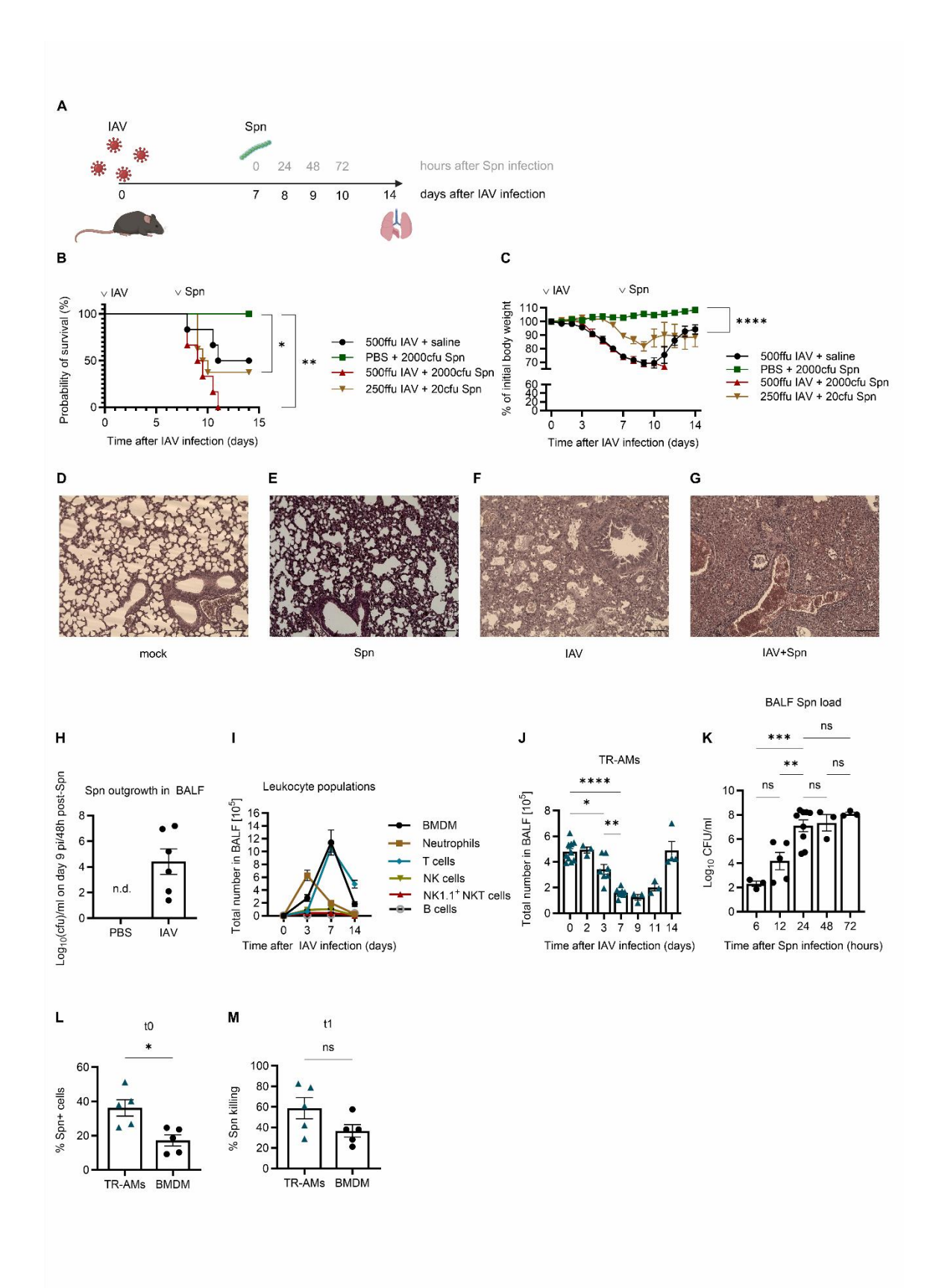


Figure 1. IAV infection increases susceptibility to secondary pneumococcal infection. (A) Schematic representation of the co-infection model, with pneumococcal infection taking place 7 days after IAV infection. (B-C) Survival (B) and weight loss (C)

after IAV/Spn co-infection of wt mice (n=6-8, data pooled from five independent experiments). (**D-G**) Representative histological images of mock-infected (**D**), Spninfected (E), IAV-infected (F), or mice infected with IAV 7 days prior to Spn infection (G), lungs harvested ten days after IAV infection. Scale bar set at 100µm, data pooled from two independent experiments. (H) Bacterial load in the BALF of IAV- or mockinfected mice nine days after IAV infection and 48h after Spn infection (mean ± SEM, n=6-9, data representative of three independent experiments). (I) Leukocyte populations including neutrophils (n=7-9), BMDM (n=8-9), NK cells (n=7-9), T cells (n=3-9), NK1.1+ NKT cells (n=3-9), and B cells (n=5-9), in the BALF of IAV-infected mice 0-14 days pi (mean ± SEM, data pooled from sixteen independent experiments). (J) TR-AM population during the IAV infection course (means ± SEM, n=3-10, data pooled from six independent experiments). (K) BALF bacterial load 6-72h after pneumococcal superinfection performed seven days post-IAV infection (mean ± SEM, n=3-9 per time point, data pooled from three independent experiments). (L-M) Spn phagocytosis capacity (L) depicted as %Spn+ cells 10min (t0) after infection and killing capacity (M, % killing at t1 over t0) for day 8 TR-AMs and BMDM, n=5, data representative of three independent experiments. Significance was determined by logrank (Mantel-Cox) test, unpaired 2-tailed t-test, and by 1-way ANOVA with Tukey's posthoc test; *p<0.05, **p<0.01, ***p <0.001, ****p <0.0001.

826

827

828

829 830

831

832

833

834 835

836 837

838839

840

841

842843

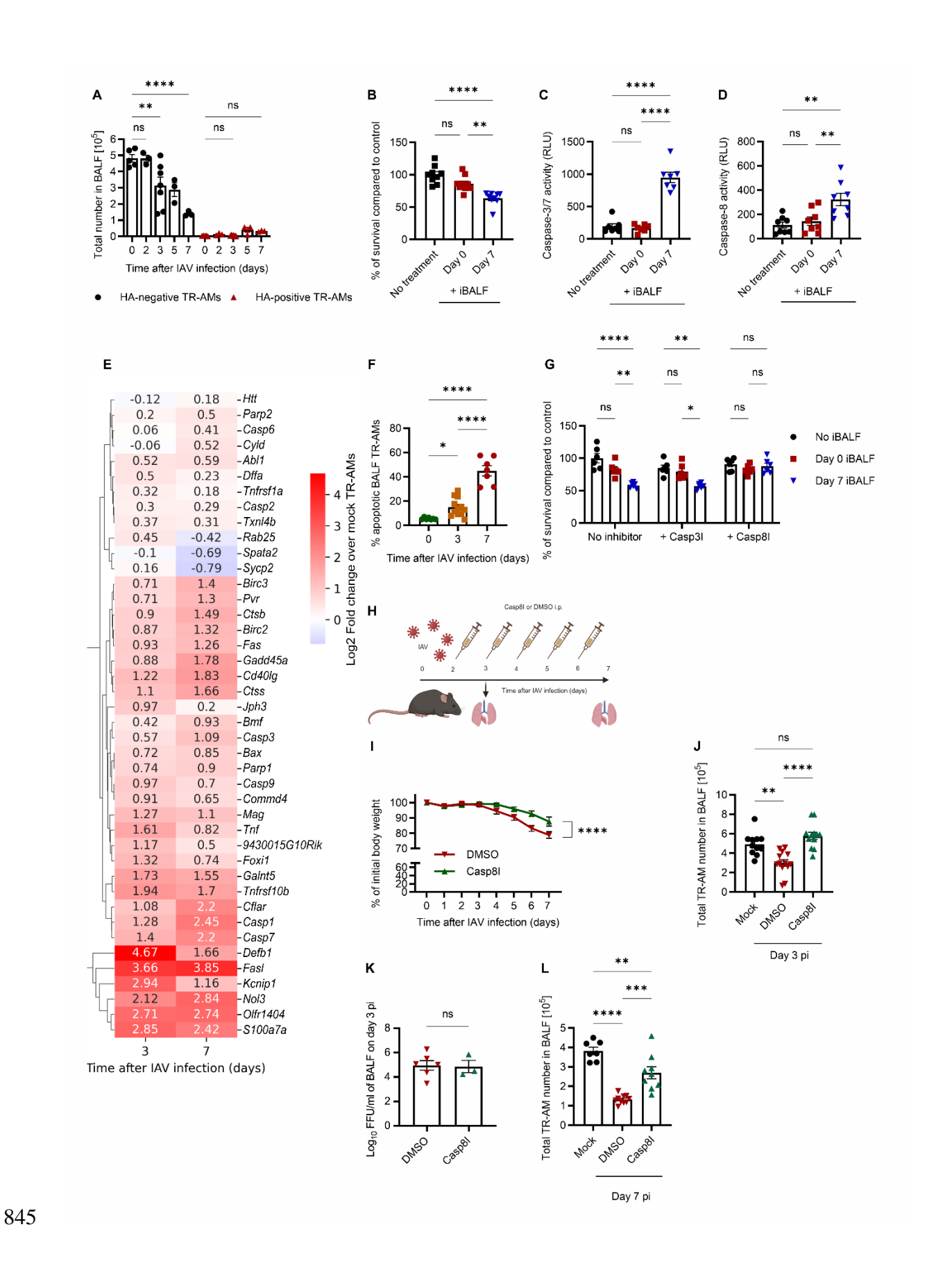


Figure 2. Caspase-8 is involved in virus-independent post-influenza TR-AM death. (A) Quantification of viral HA-negative and HA-positive TR-AMs after IAV infection, mean ± SEM is depicted, n=3-7, data pooled from three independent experiments. (B) TR-AM survival following 24h treatment with iBALF. Graphs

represent means ± SEM, n=9 per group, data pooled from three independent experiments. (C-D) Caspase-3/7 (C) and caspase-8 activity (D) after iBALF TR-AM treatment. Graphs represent means ± SEM, n=7-8, data pooled from three independent experiments, respectively. (E) Heat map depicting average fold changes of cell death-related genes in flow-sorted, HA-negative, mock, day 3, and day 7 pi BALF TR-AMs, n=3-7 per time point, data pooled from four independent experiments. (F) Percentage of apoptotic TR-AMs on days 0, 3, and 7 pi (means ± SEM, n=7-12, data pooled from four independent experiments). (G) Colorimetric viability assay following naïve TR-AM treatment with iBALF after 3h pre-treatment with 50µM of a specific caspase inhibitor (means ± SEM, n=6). Data pooled from two independent experiments. (H) Experimental layout for caspase-8 inhibition in vivo experiments. (I) Weight loss after IAV infection and caspase-8 inhibition, n=8-11, data pooled from six independent experiments. (J) BALF TR-AMs on day 3 pi after in vivo caspase-8 inhibition (means ± SEM, n=11-13, data pooled from four independent experiments). (K). BALF viral titers on day 3 pi after in vivo caspase-8 inhibition (means ± SEM, n=3-6, data pooled from two independent experiments). (L) BALF TR-AMs on day 7 pi after in vivo caspase-8 inhibition (means ± SEM, n=7-10, data pooled from seven independent experiments. Significance was determined by 2-tailed t-test of the Areas Under Curve (AUC) for the compared groups in (I), 1-way, or 2 -way ANOVA with Tukey's posthoc test; *p<0.05, **p<0.01, ***p <0.001, ****p <0.0001.

850

851 852

853

854855

856

857

858859

860

861 862

863 864

865

866

867868

869

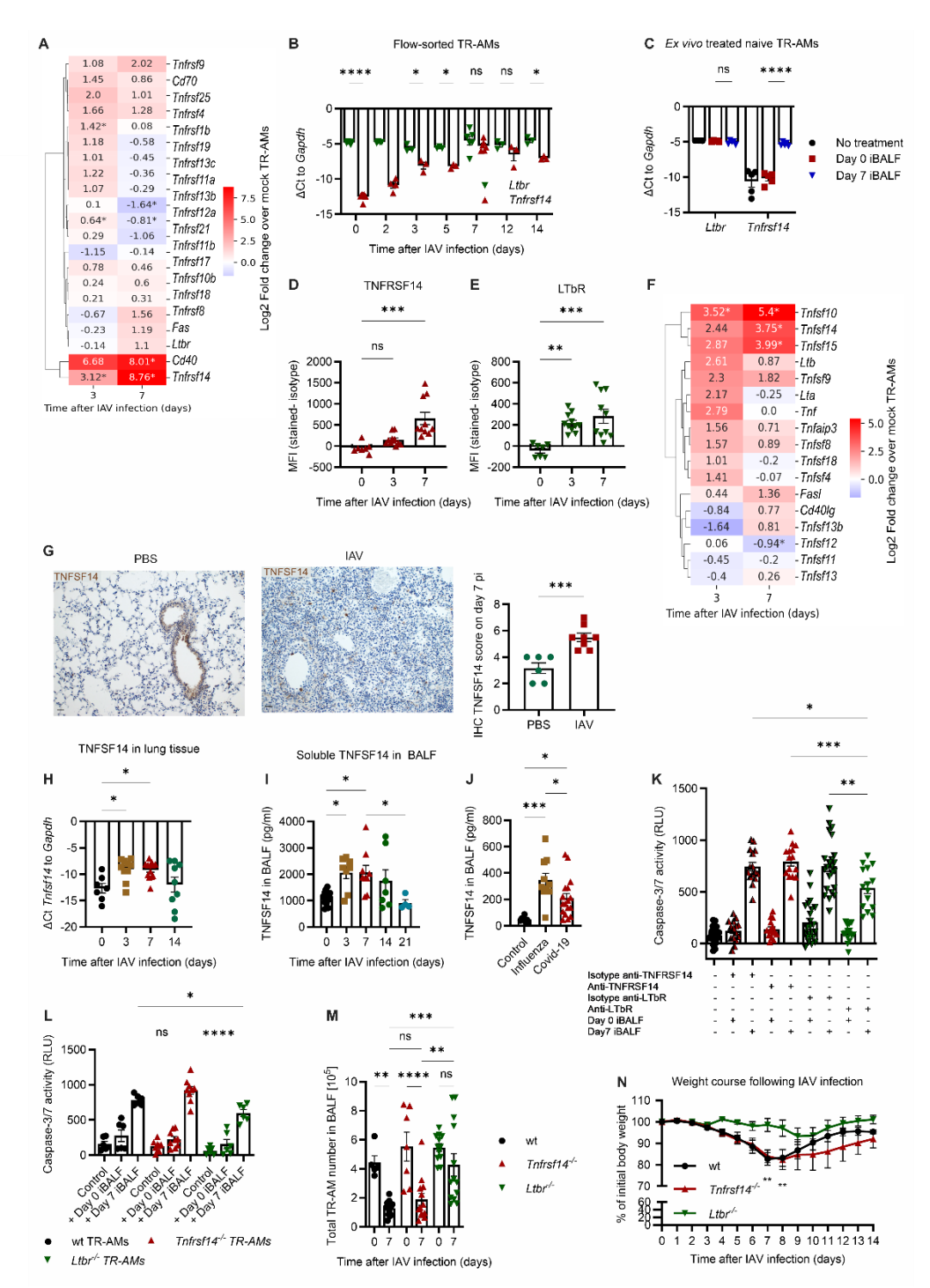


Figure 3. IAV infection leads to an increased expression of the TNFSF14 ligand-receptor axis. (**A**) Fold change of TNFSF receptor genes in mock, day 3, and day 7 TR-AMs (n=5-6, data pooled from three experiments). (**B**) TR-AM *Tnfrsf14* and *Ltbr* gene expression over IAV infection course, n=3-6, data pooled from two experiments. (**C**) TR-AM *Tnfrsf14* and *Ltbr* gene expression after ex vivo iBALF treatment (n=5, data representative of three experiments). (**D-E**) TR-AM TNFRSF14 (**D**) and LTbR (**E**) expression (n=7-11, data pooled from six experiments). (**F**) Fold change of TNFSF ligand genes in mock, day 3, and day 7 TR-AMs (n=5-6, data pooled from three independent experiments). (**G**) IHC analysis for TNFSF14 expression after mock (PBS) or IAV infection. Scale bar set at 25μm (n=6-8, data pooled from two experiments). (**H**) *Tnfsf14* gene expression in the lungs of IAV-infected animals (n=7-8, data pooled from three experiments). (**I**) BALF TNFSF14 measured by ELISA (n=4-

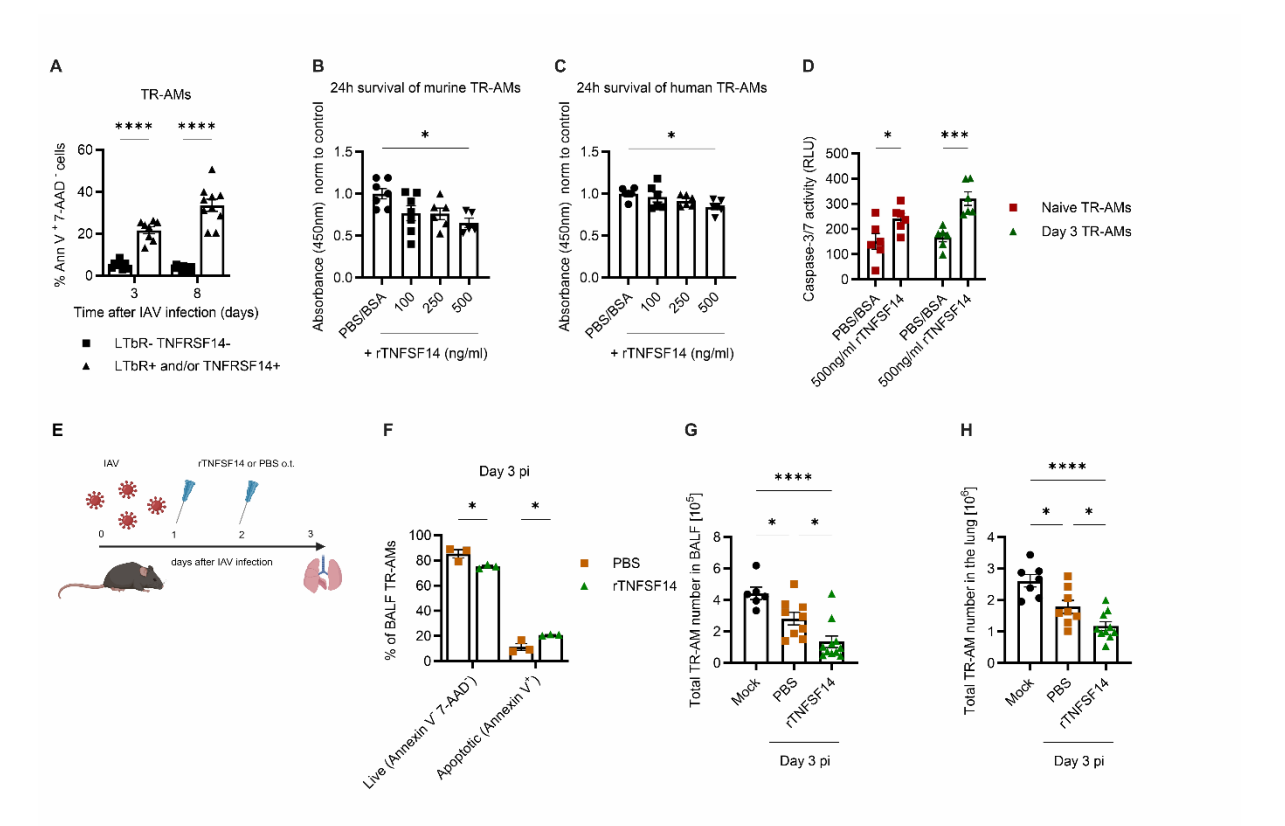


Figure 4. TNFSF14 treatment aggravates post-influenza TR-AM loss. (A) Percentage of apoptotic cells within LTbR⁻ TNFRSF14⁻ and LTbR⁺ and/or TNFRSF14⁺ TR-AM subgroups on days 3 and 8 pi. Graphs represent means ± SEM, n=8-10 per group, data pooled from two independent experiments. (B-C) Cell survival proportional to light absorbance after 24h treatment of murine (B) and human (C) TR-AMs with different doses of rTNFSF14 and normalized to control samples. Graph represents means ± SEM, n=5-7. Data in (B) and (C) pooled from seven and four independent experiments, respectively. (D) Caspase-3/7 activity after 24h TR-AM treatment with 500ng/ml rTNFSF14 (means ± SEM, n=6-7, data pooled from six independent experiments). (E) Schematics of rTNFSF14 application to IAV-infected mice days 1 and 2 pi with analysis performed on day 3 pi. (F) Percentage of live (annexin V-7-AAD-) and apoptotic (annexin V+7-AAD-) TR-AMs (n=3) on day 3 pi after rTNFSF14 treatment, data representative of three different experiments. (G-H) Total BALF (n=6-11, **G**) and lung-tissue TR-AMs (n=7-10, **H**) on day 3 pi after rTNFSF14 treatment, compared to mock infection. Graphs represent means ± SEM and data is pooled from seven independent experiments. Significance was determined by 1-way or 2-way ANOVA with Tukey's posthoc test; *p<0.05, **p<0.01, ***p <0.001, ****p <0.0001.

898 899

900

901

902

903

904

905

906

907

908

909

910

911

912

913

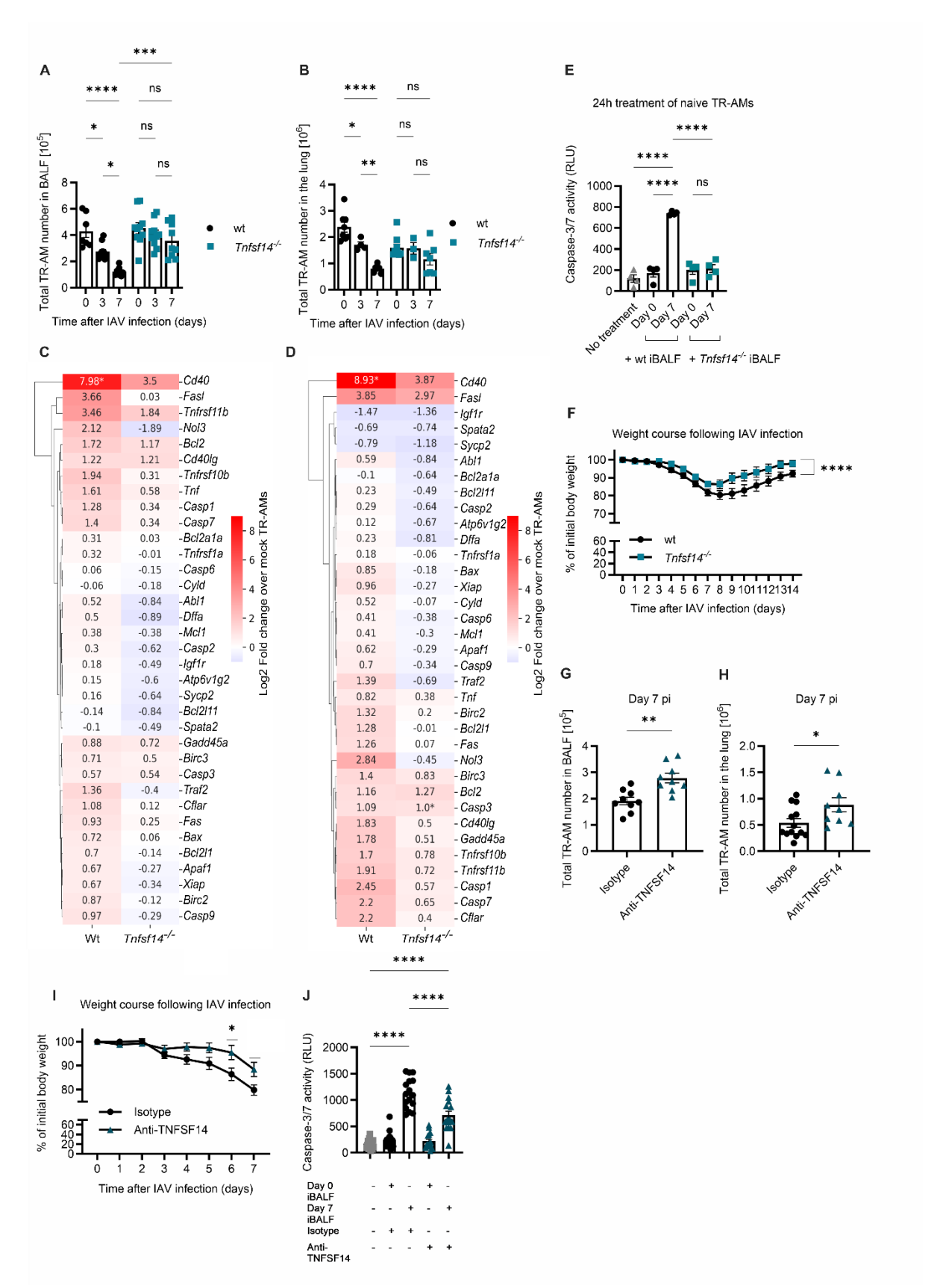


Figure 5. Post-influenza TR-AM loss can be prevented through directed targeting of the TNFSF14 ligand. (**A-B**) BALF TR-AMs (**A**) and sessile lung TR-AMs (**B**) in wt and *Tnfsf14*-- mice after IAV infection (means ± SEM, n=8-12, data pooled from seventeen different experiments, wt controls in (**B**) including values depicted in Supplemental Figure 2A). (**C-D**) Heat maps depicting fold change of apoptosis-related

genes on day 3 pi (C) and day 7 pi (D) over mock-infected wt and Tnfsf14--TR-AMs, n=3-5, data pooled from five different experiments. Wt data extracted from the data set presented in Figure 2E. (E) Caspase-3/7 activity after TR-AM treatment with wt and Tnfsf14-- iBALF. Graph represents means ± SEM, n=4 per condition, data representative of three independent experiments. (F) Body weight of wt and Tnfsf14-/mice over the IAV infection course. Graph represents means ± SEM of weight at each time point, n=12-13, data pooled from six independent experiments, wt controls including data presented in Figure 3M). (G-H) BALF (G) and lung tissue (H) TR-AMs on day 7 pi after anti-TNFSF14 treatment on day 2 pi. Graph represents means ± SEM, n=9-13, data pooled from four independent experiments. (I) Body weight of anti-TNFSF14 and isotype-treated wt mice after IAV infection. Graph represents means ± SEM of weight at each time point, n=10-11, data pooled from four independent experiments. (J) Caspase-3/7 activity after 24h iBALF treatment of anti-TNFSF14 pretreated naïve TR-AMs. Data pooled from six independent experiments (means ± SEM, n=16). Significance was determined by unpaired 2-tailed t-test, 1-way, or 2-way ANOVA with Tukey's posthoc test; *p<0.05, **p<0.01, ***p <0.001, ****p <0.0001.

921 922

923

924

925

926

927

928 929

930

931

932

933934

935

936

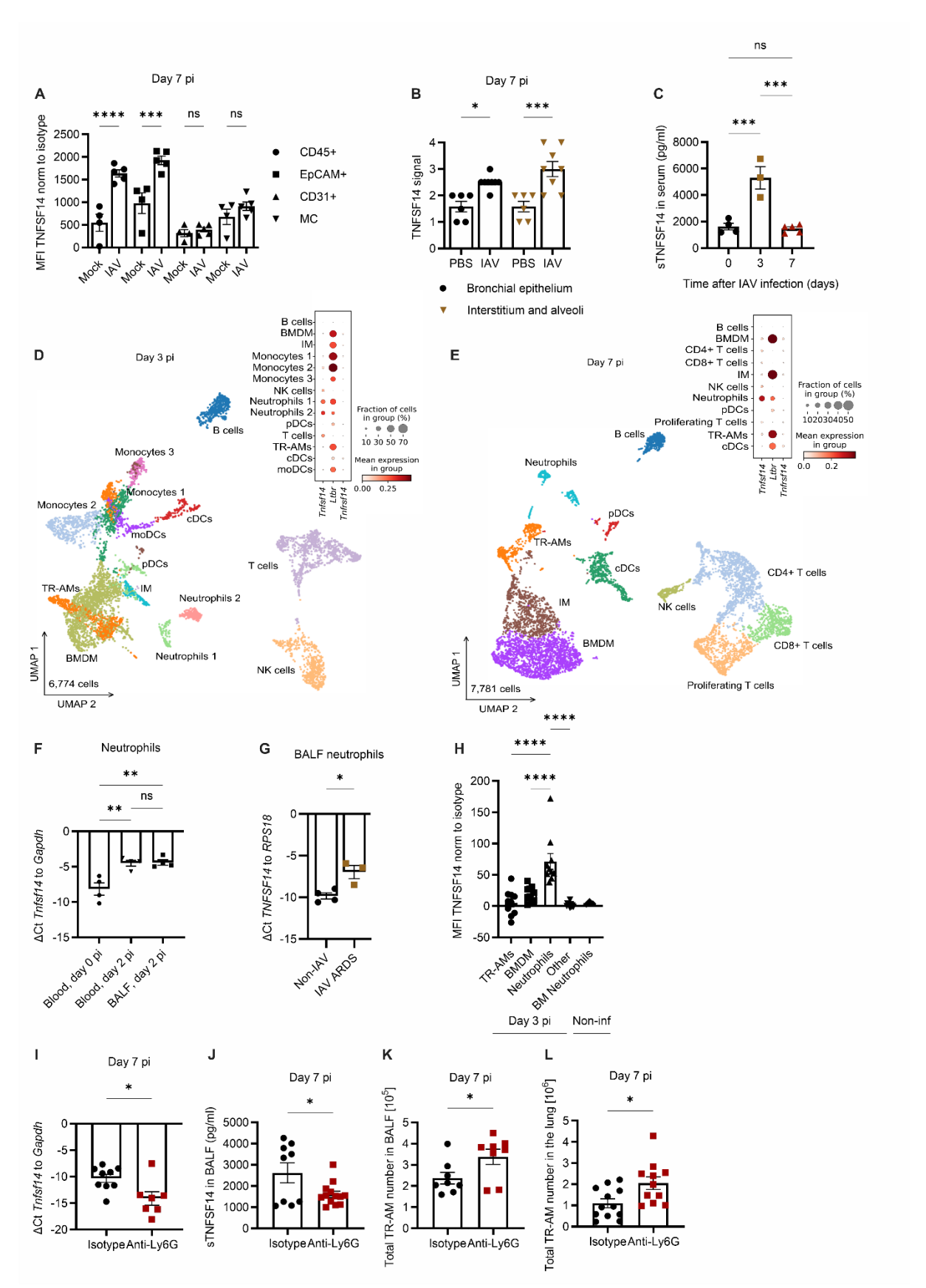


Figure 6. Neutrophils are the main cellular source of TNFSF14 during IAV infection. (A) TNFSF14 expression on leukocytes, epithelial, endothelial cells, and MC in the lungs of non-infected and day 7 mice, n=4-5, data pooled from two independent experiments. (B) TNFSF14 expression in different lung regions of mock-

and IAV-infected wt mice on day 7 pi (n=3-4, data representative of two independent experiments). Scale bar set at 25µm. (C) Serum TNFSF14 on days 0, 3, and 7 pi (n=3-5, data pooled from three independent experiments). (D-E) Leukocyte scRNA-Seg analysis on day 3 (**D**) and day 7 pi (**E**), n=4, data from two independent experiments. Monocyte and neutrophil clusters on day 3 pi were characterized according to the gene signature of the top 5 uniquely expressed genes per cluster. Dot plots depict *Tnfsf14*, Ltbr, and Tnfrsf14 expression. (F) qPCR analysis for Tnfsf14 expression in blood and BALF neutrophils (n=4, data pooled from two independent experiments). (G) qPCR analysis for TNFSF14 expression in BALF neutrophils from patients with severe IAVinduced ARDS compared to non-IAV controls (n=3-4). (H) TNFSF14 expression on BALF leukocytes on day 3 pi and bone marrow-derived (BM) neutrophils from noninfected mice, n=3-10, data pooled from two independent experiments. (I-J) qPCR analysis in lung tissue, n=7-9 (I), and BALF ELISA, n=9-13 (J), for TNFSF14 expression on day 7 pi after neutrophil depletion. Data pooled from four and five independent experiments, respectively. (K-L) BALF (K) and lung (L) TR-AMs on day 7 pi after neutrophil depletion (n=8, data pooled from four and five independent experiments, respectively). Graphs represent means ± SEM. Significance was determined by unpaired 2-tailed t-test, 1-way, or 2-way ANOVA; *p<0.05, **p<0.01, ***p <0.001, ****p <0.0001.

943

944

945

946

947

948

949

950

951952

953954

955

956 957

958

959

960

961

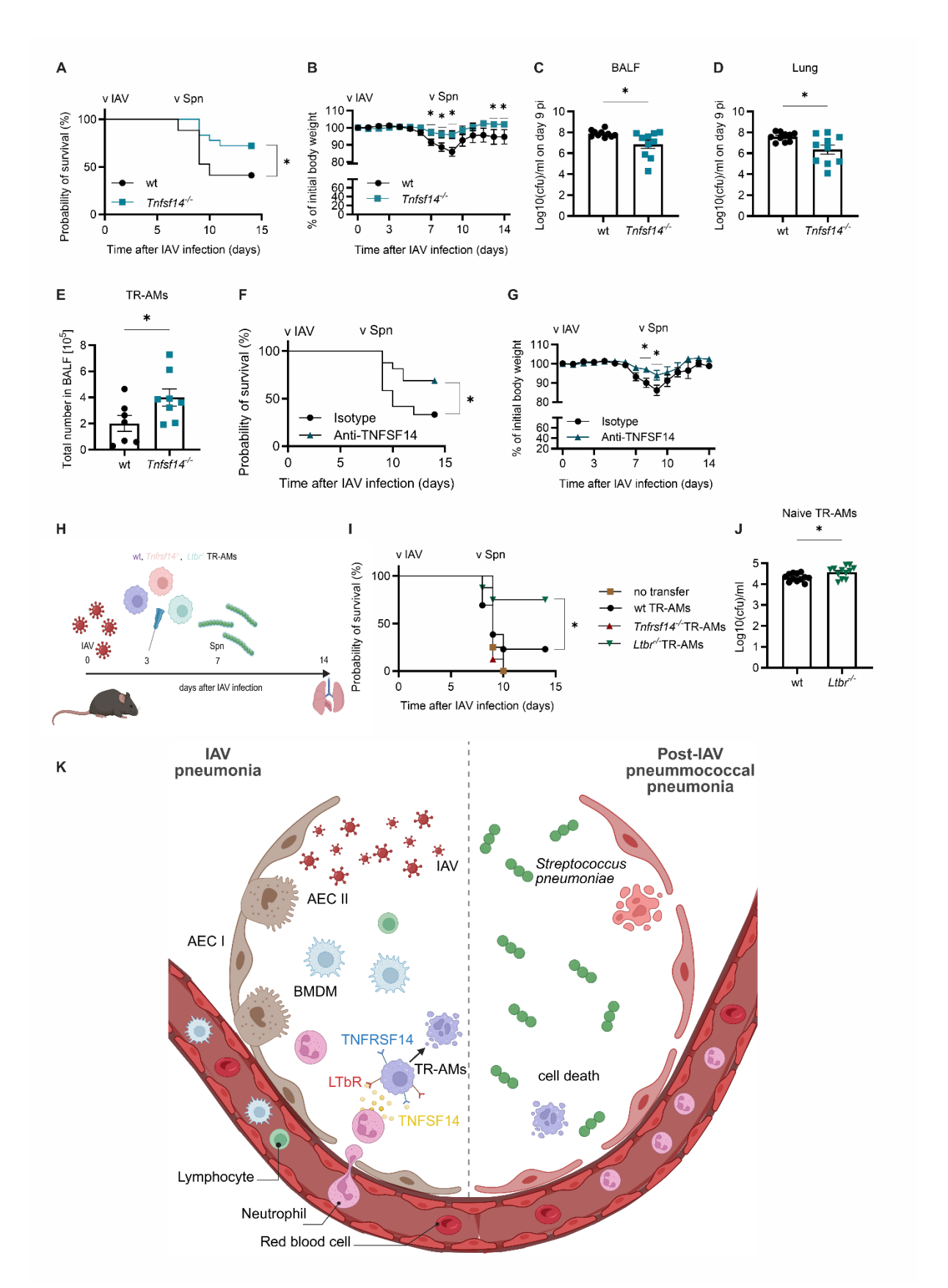


Figure 7. Severity of post-influenza pneumococcal pneumonia is attenuated in the absence of TNFSF14. (**A-B**) Survival (**A**) and weight loss (**B**) after IAV/Spn coinfection of wt and *Tnfsf14*-/- mice (means ± SEM, n=17-18, data pooled from five different experiments). (**C-D**) Bacterial burden in the BALF (**C**) and in the lungs (**D**) of wt and *Tnfsf14*-/- mice 9 days after IAV infection and 48h after Spn infection (means ±

SEM, n=10, data pooled from eight independent experiments). (E) Total BALF TR-AM numbers of wt and Tnfsf14-/- mice 9 days after IAV/ 48h after Spn infection (means ± SEM, n=7-8, data pooled from five different experiments). (F-G) Survival (F) and weight loss (G) following IAV/Spn co-infection and TNFSF14 blocking on day 2 pi (means ± SEM, n=12-16, data pooled from five independent experiments). (H) Schematics of experimental layout for IAV/Spn co-infection with adoptive transfer (a.t.) of naïve wt, Tnfrsf14^{-/-}, or Ltbr^{-/-} TR-AMs on day 3 pi. (I) Survival of wt mice upon IAV/Spn coinfection and TR-AM a.t. (means ± SEM, n=4-12, data pooled from five independent experiments). (J) Bacterial load in lysed wt and Ltbr/- naïve TR-AMs after ex vivo Spn infection (means ± SEM, n=12, data pooled from four independent experiments). Significance was determined by log-rank (Mantel-Cox) test, unpaired 2-tailed t-test, 1way and 2-way ANOVA with Tukey's posthoc test; *p<0.05, **p<0.01. (K) Proposed hypothesis: Severe IAV-induced pneumonia is characterized by massive leukocyte recruitment, including neutrophils. Once in the alveoli, neutrophils start releasing TNFSF14, which is sensed by TR-AMs through ligation to surfaced-expressed receptors TNFRSF14 and LTbR, culminating in TR-AM death, which increases host susceptibility to post-influenza pneumococcal pneumonia. AEC: alveolar epithelial cells.

969

970

971

972973

974

975

976 977

978

979

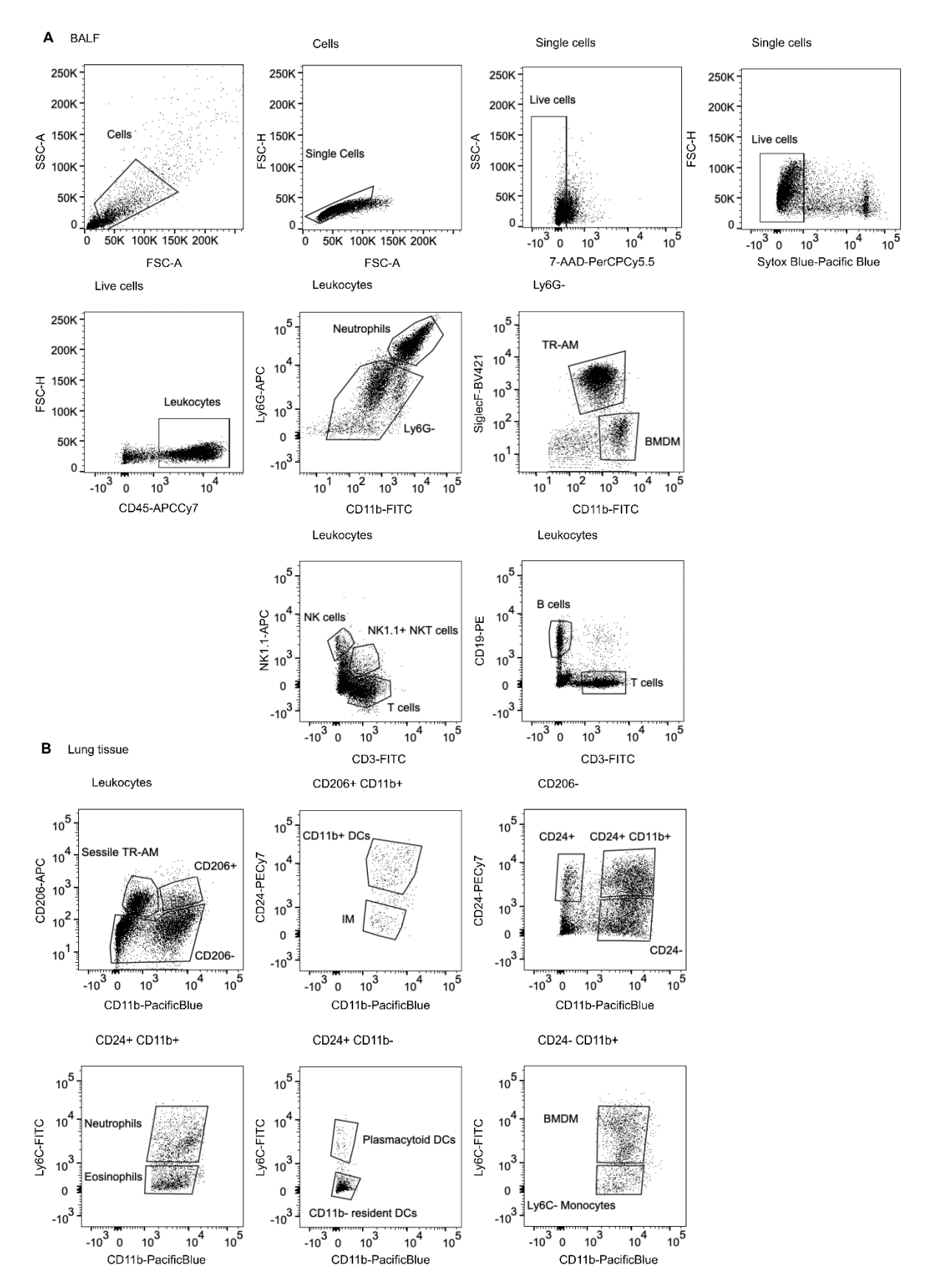
980 981

982

983

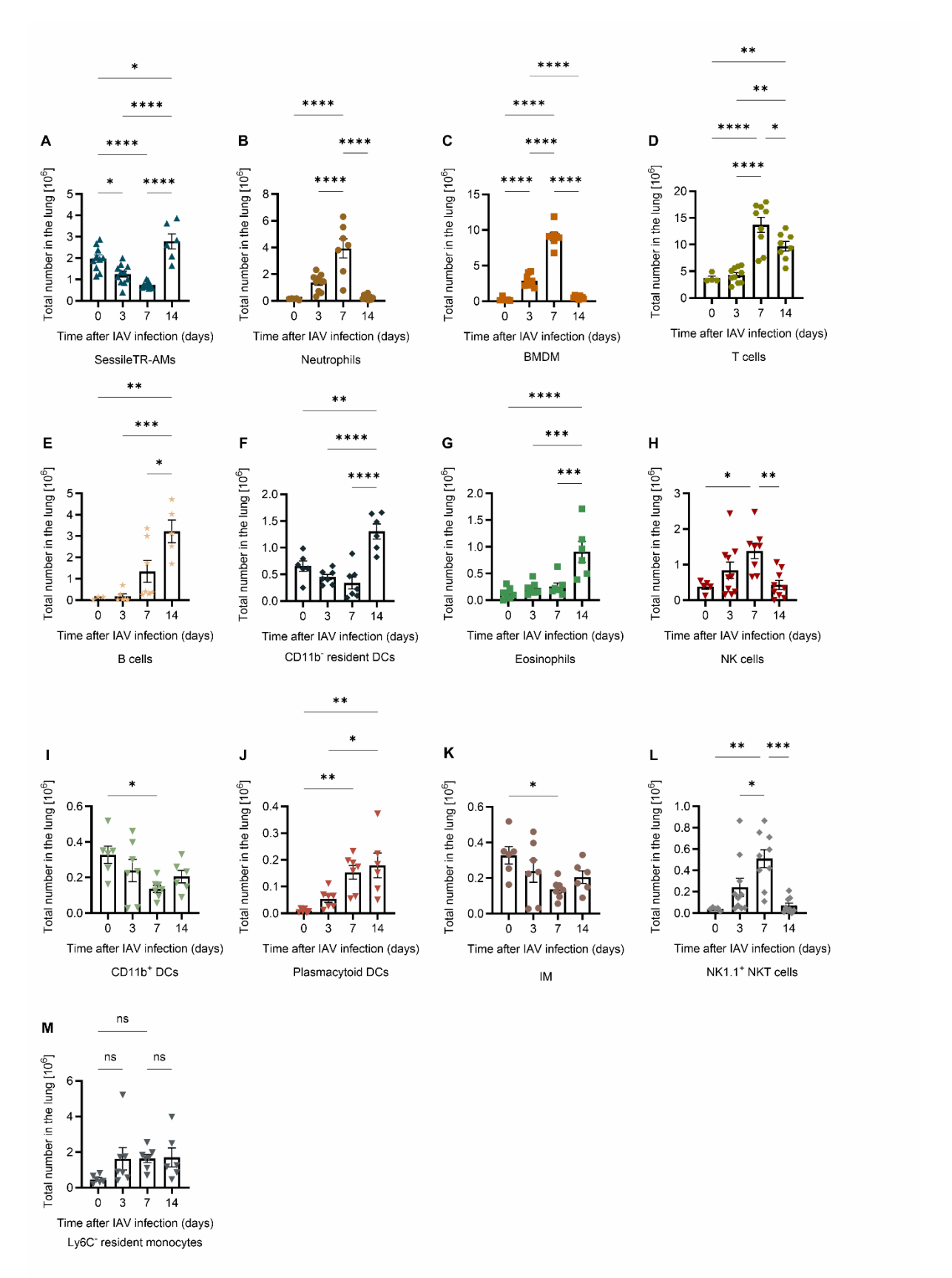
984 985

986



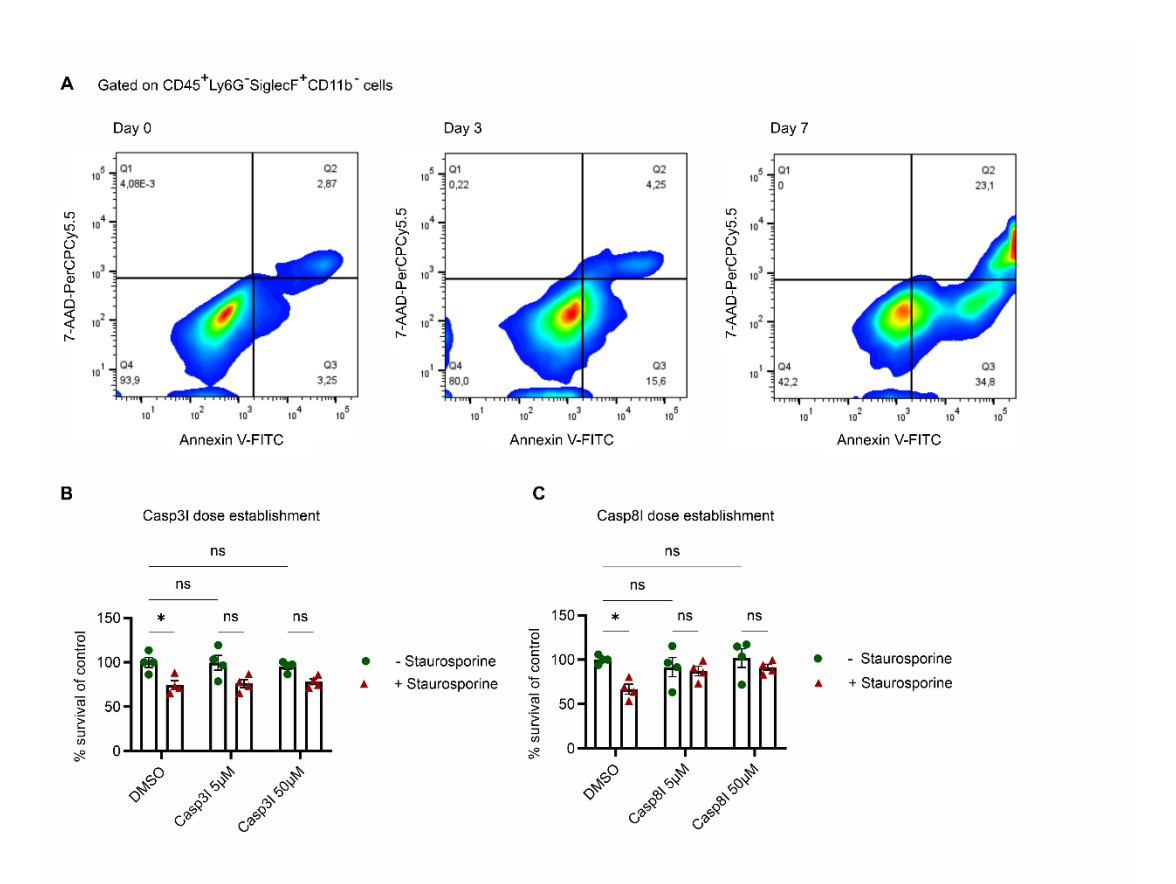
Supplemental Figure 1. Gating strategy for the identification of different immune cell populations in murine BALF (A) and lung tissue (B) per flow cytometry analysis. Representative plots following multicolor staining of BALF and lung-tissue immune cells, as described in the 'Supplemental Methods' document. Gating

strategies were set according to the appropriate isotype and fluorescence minus one (FMO) controls.

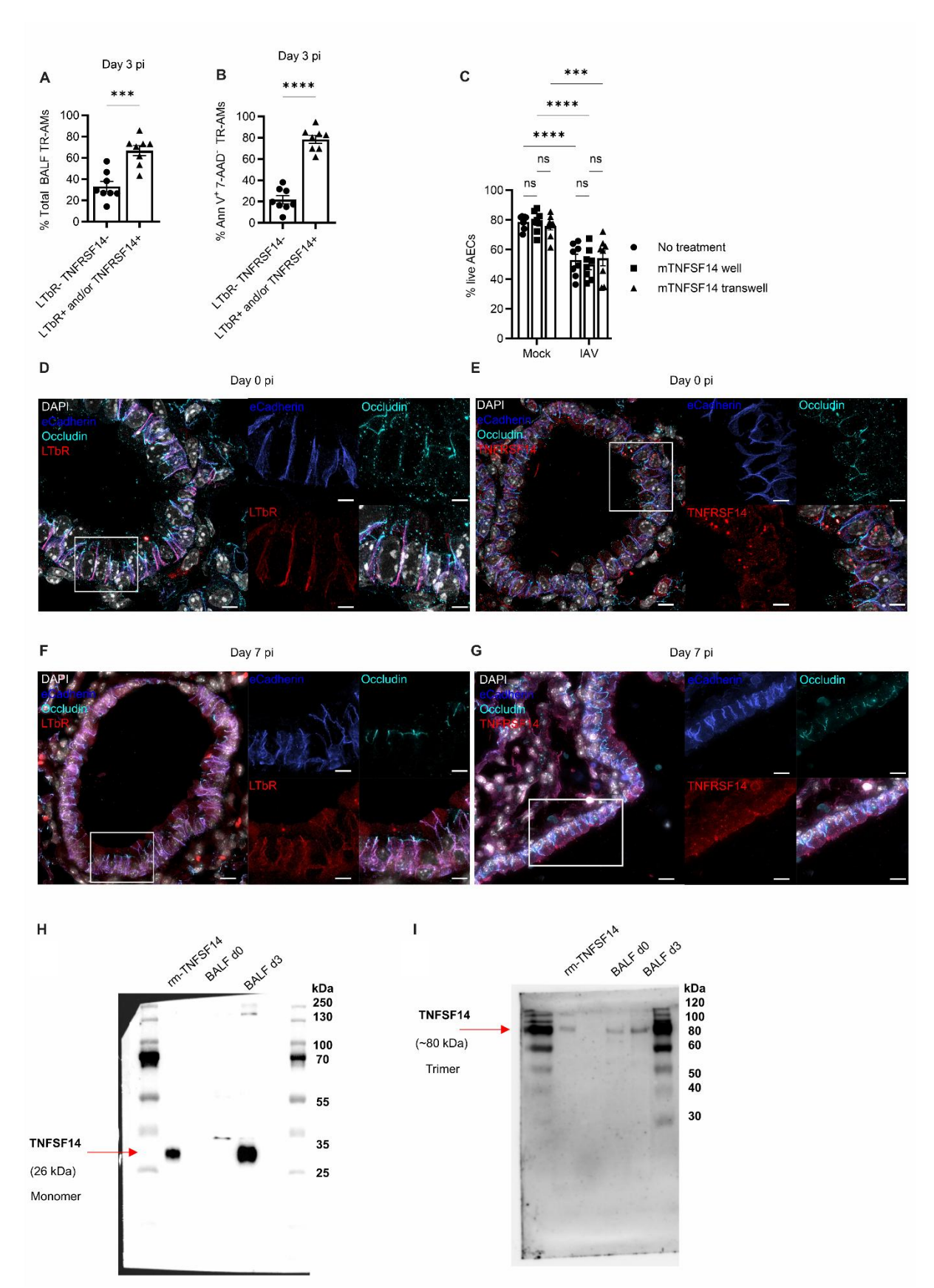


Supplemental Figure 2. Immune cell kinetics in the lung tissue of IAV-infected mice over the infection course. Following BALF extraction, lungs of wild-type mice infected with 500ffu IAV were harvested at different time points. Immune cell populations were identified per flow cytometry analysis, including sessile TR-AMs (n=6-11) (A), neutrophils (n=5-10) (B), BMDM (n=5-10) (C), T cells (n=4-10) (D), B

cells (n=3-7) (**E**), CD11b⁻ resident DCs, (n=6-7) (**F**), eosinophils (n=6-7) (**G**), NK cells (n=5-10) (**H**), CD11b⁺ DCs (n=6-7) (**I**), pDCs (n=6-7) (**J**), IM (n=6-7) (**K**), NK1.1⁺ NKT cells (n=5-10) (**L**), and Ly6C⁻ resident monocytes (n=6-7) (**M**). Data shown pooled from nine independent experiments, mean ± SEM is depicted. Significance was determined by 1-way ANOVA with Tukey's posthoc test; *p<0.05, **p<0.01, ***p<0.001, ****p<0.001. (p)DCs: (plasmacytoid) dendritic cells, IM: interstitial macrophages, NK: natural killer.

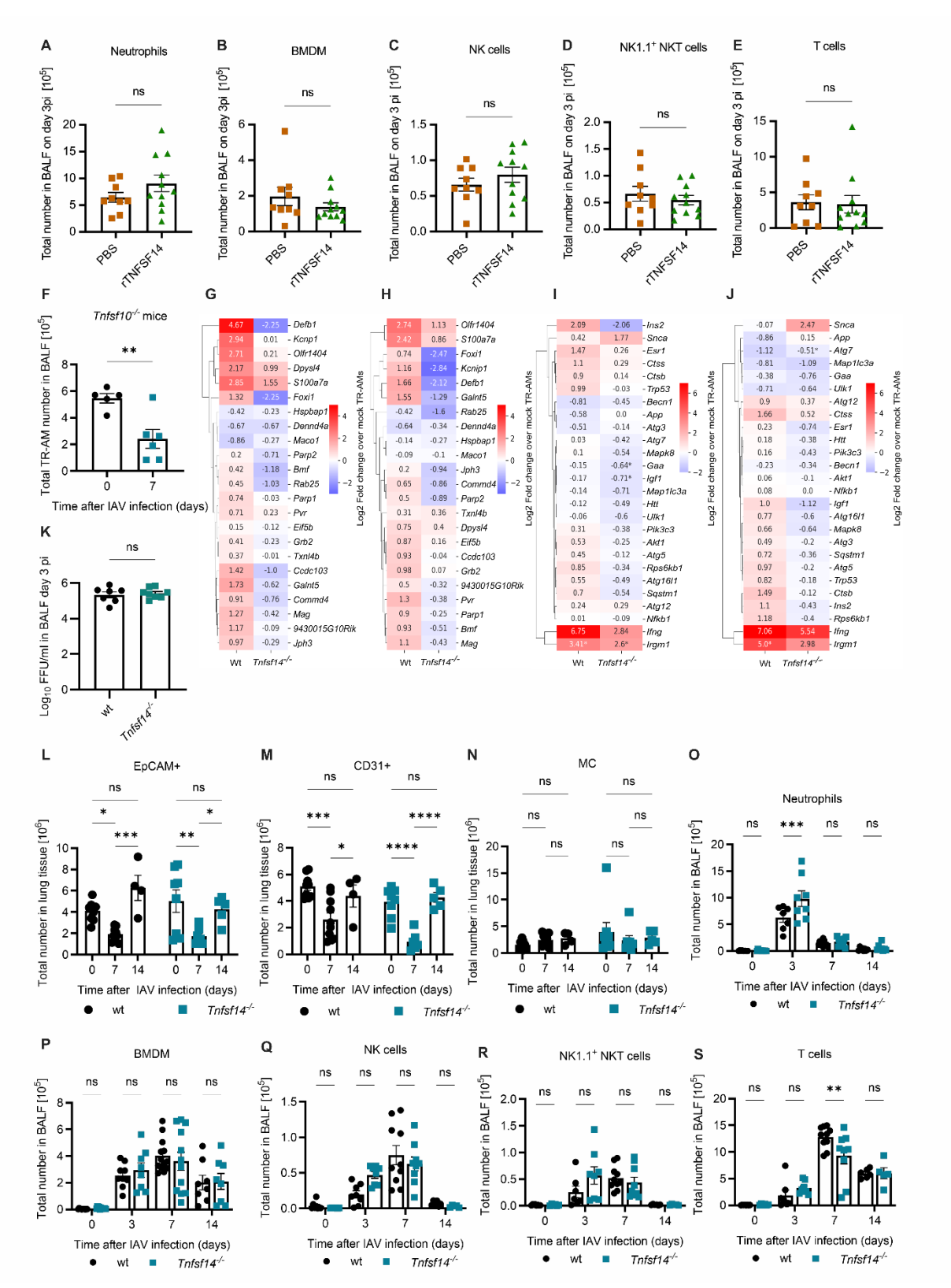


Supplemental Figure 3. TR-AM apoptosis can be attenuated through the use of a caspase inhibitor. (A) Gating strategy for the quantification of apoptotic TR-AMs in the BALF of IAV-infected mice on days 0, 3, and 7 pi. (B-C) TR-AM viability following treatment with 0.5 μ M staurosporine and different doses of a caspase-3 (B) or a caspase-8 (C) inhibitor, values depicted as % survival of control. DMSO-treated cells set at 100%. Graphs represent means \pm SEM, n=4 per condition. Data pooled from three independent experiments. Significance was determined by 2-way ANOVA with Tukey's posthoc test; *p<0.05.



Supplemental Figure 4. TNFSF14 orchestrates post-influenza TR-AM apoptosis in a cell-specific manner. (**A-B**) TNFSF14 receptor- positive cells as percentage of all BALF TR-AMs on day 3 pi (**A**) and percentage of apoptotic TR-AMs based on TNFSF14 receptor expression at the same time point (**B**). Graphs represent means ±

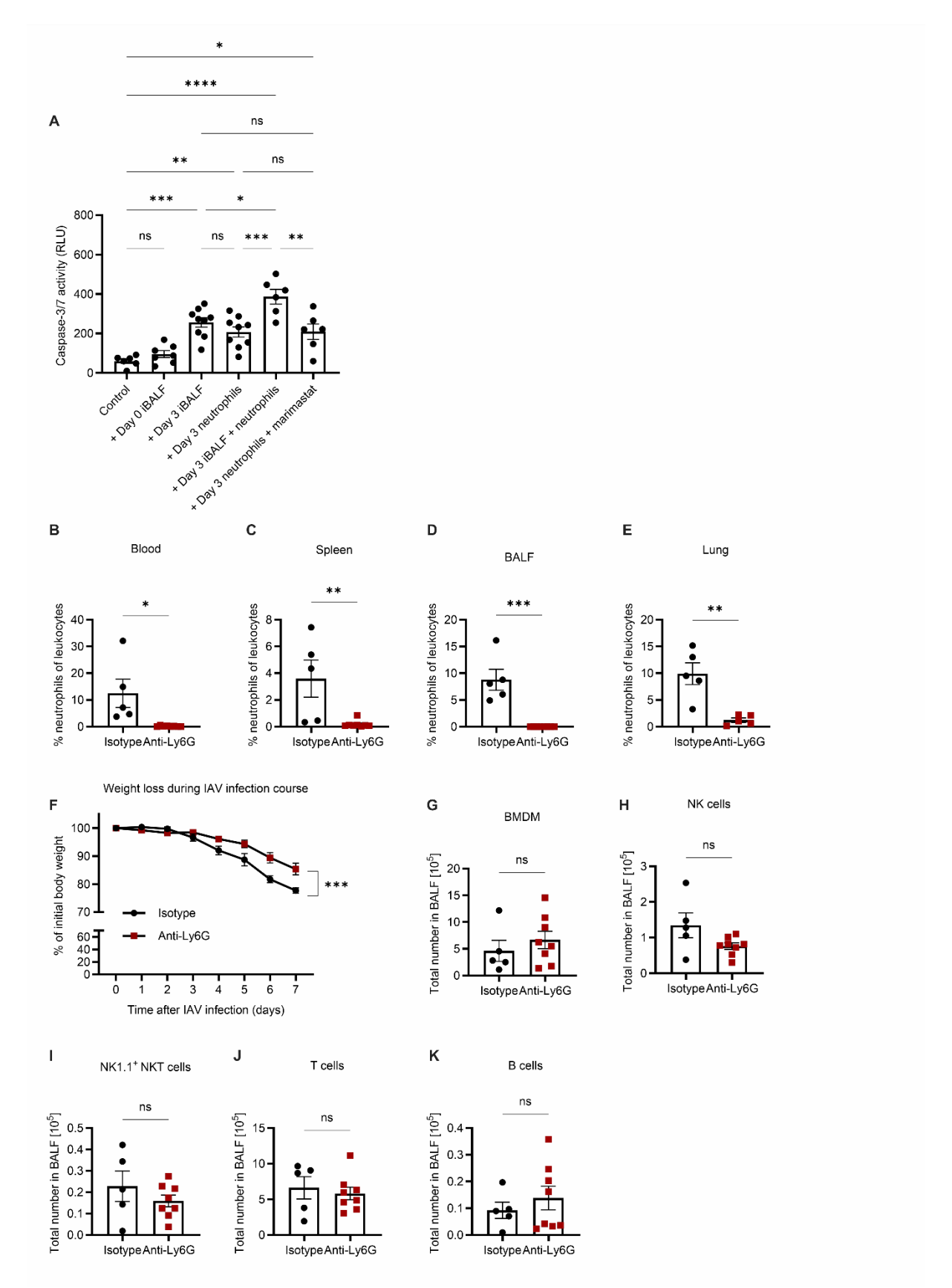
SEM, n=8 per group, data poled from two independent experiments. (**C**) Percentage of live transwell-seeded AEC after 24h IAV infection and treatment with rTNFSF14. Graphs represent means \pm SEM, n=9 per group, data pooled from two independent experiments. (**D-G**) Immunofluorescence analysis revealing a basolateral LTbR expression (**D,F**) and a non-preferential, cytoplasmic TNFRSF14 expression (**E,G**) on epithelial cells on days 0 (**D-E**) and 7 pi (**F-G**). Scale bar for smaller panels set at 5 μ m, for larger panels set at 10 μ m (**D-E**) or 20 μ m (**F-G**). Data representative of three independent experiments. (**H-I**) SDS-PAGE (**H**) and blue native PAGE (**I**) for TNFSF14 in naïve and day 3 BALF samples with mouse rTNFSF14 (rmTNFSF14) as a positive control, demonstrating a single band at 26kDa upon denaturation. Under naïve conditions TNFSF14 appeared around 80kDa, reflecting the presence of the homotrimer in the BALF. Data representative of three independent experiments. Graphs represent means \pm SEM, n=6-8. Data pooled from three independent experiments. Significance was determined by unpaired 2-tailed t-test and two-way ANOVA; ***p <0.001, ****p <0.0001.



Supplemental Figure 5. Lack of TNFSF14 attenuates TR-AM death without heavily affecting other cell population kinetics. (**A-E**) BALF neutrophils (**A**), BMDM (**B**), NK cells (**C**), NK1.1+ NKT cells (**D**), and T cells (**E**) on day 3 pi after rTNFSF14 treatment on days 1 and 2, n=9-11, means ± SEM, data pooled from three independent experiments. (**F**) Quantification of TR-AM numbers in the BALF of IAV-infected *Tnfsf10*-/- mice on day 7 pi (means ± SEM, n=5-6, data pooled from three independent experiments). (**G-J**) Heat maps depicting fold change of necrosis- (**G-H**) and

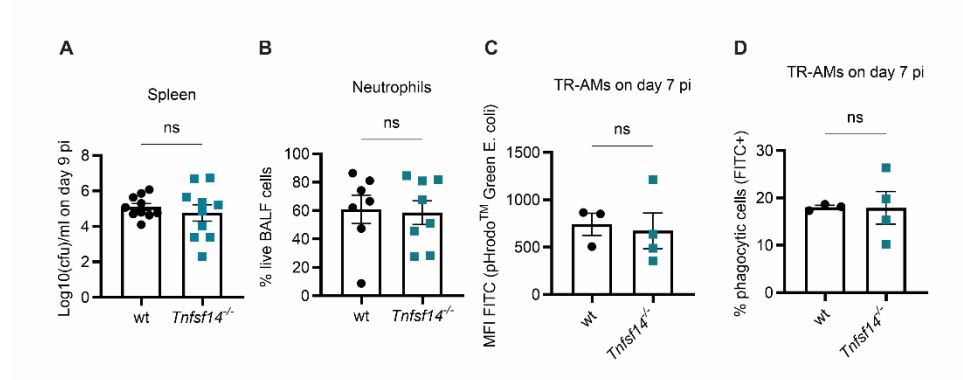
 $\begin{array}{c} 1043 \\ 1044 \end{array}$

autophagy-related (**I-J**) genes on day 3 pi (**G**, **I**) and day 7 pi (**H**, **J**) over mock-infected wt and *Tnfsf14*-/- TR-AMs, n=3-5, data from five independent experiments. Wt data extracted from the data set presented in Figure 2E. (**K**) Viral titers in the BALF of wt and *Tnfsf14*-/- mice on day 3 pi (means ± SEM, n=4, data representative of three independent experiments). (**L-N**) Lung epithelial (EpCAM+, **L**), endothelial (CD31+, **M**), and mesenchymal cells (MC, **N**) of wt and *Tnfsf14*-/- mice after IAV infection (means ± SEM, n=4-10, data pooled from ten independent experiments). (**O-S**) Immune cell populations in the BALF of wt and *Tnfsf14*-/- mice, including neutrophils (**O**), BMDM (**P**), NK cells (**Q**), NK1.1+ NKT cells (**R**), and T cells (**S**). Graphs represent means ± SEM, n=5-13, data pooled from fourteen independent experiments, wt controls including data presented in Figure 1I. Significance was determined by unpaired 2-tailed t-test and 2-way ANOVA with Tukey's posthoc test; *p<0.05, **p<0.01, ****p<0.001, *****p<0.0001.



Supplemental Figure 6. Neutrophil depletion attenuates weight loss without affecting leukocyte influx after IAV infection. (A) Caspase-3/7 activation after treatment of day 3 TR-AMs with iBALF or co-culture with neutrophils plus a metalloproteinase inhibitor, n=6-9, data pooled from three independent experiments. (B-E) Neutrophils depicted as percentage of total leukocyte numbers after neutrophil

depletion, in the blood (**B**), spleen (**C**), BALF (**D**), and lungs (**E**) of IAV-infected mice on day 7 pi (means ± SEM, n=5-8, data pooled from two independent experiments). (**F**) Body weight as percentage of initial weight after IAV infection and neutrophil depletion, n=7-11, data pooled from four independent experiments. (**G-K**) BALF immune populations on day 7 pi after neutrophil depletion, including BMDM, (**G**), NK cells (**H**), NK1.1⁺ NKT cells (**I**), T cells (**J**), and B cells (**K**). Graphs represent means ± SEM, n=5-8, data from two independent experiments. Significance was determined by unpaired 2-tailed t-test for two groups, including the AUC between the two treatment groups for (**F**); *p<0.05, **p<0.01, ***p<0.001, ****p<0.0001.



Supplemental Figure 7. Loss of TNFSF14 does not impact neutrophil influx, spleen bacterial burden, or TR-AM phagocytosis capacity after IAV/Spn co-infection. (A) Spn burden in the spleens of wt and *Tnfsf14*-- mice 9 days after IAV infection and 48h after Spn infection (means ± SEM, n=10, data pooled from eight different experiments). (B) Neutrophils depicted as percentage of total live cells in the BALF of wt and *Tnfsf14*-- mice at the same time point (means ± SEM, n=7-8, data pooled from five independent experiments). (C-D) Phagocytosis capacity of wt and *Tnfsf14*-- day 7 TR-AMs depicted as FITC signal normalized to non-infected TR-AMs (C) and percentage of FITC+ TR-AMs (phagocytic cells, D), following ex vivo incubation with pHrodoTM Green *Escherichia coli* BioParticlesTM (means ± SEM, n=3-4, data representative of three independent experiments). Significance was determined by unpaired 2-tailed t-test.